

ORIGINAL ARTICLE

A robust, four-node, quadrilateral element for stress analysis of functionally graded plates through higher-order theories

G. M. Kulikov^a, S. V. Plotnikova^a, and E. Carrera^b

^aLaboratory of Intelligent Materials and Structures, Tambov State Technical University, Tambov, Russia; ^bDepartment of Aeronautics and Aerospace Engineering, Politecnico di Torino, Torino, Italy

ABSTRACT

A hybrid-mixed, four-node, quadrilateral element for the three-dimensional (3D) stress analysis of functionally graded (FG) plates using the method of sampling surfaces (SaS) is developed. The SaS formulation is based on choosing an inside the plate body N , not equally spaced SaS parallel to the middle surface, in order to introduce the displacements of these surfaces as basic plate variables. Such a choice of unknowns, with the consequent use of Lagrange polynomials of the degree $N - 1$ in the assumed distributions of displacements, strains, and mechanical properties through the thickness leads to a robust FG plate formulation. All SaS are located at Chebyshev polynomial nodes that permit one to minimize uniformly the error due to the Lagrange interpolation. To avoid shear locking and spurious zero-energy modes, the assumed natural strain method is employed. The proposed four-node quadrilateral element passes 3D patch tests for FG plates and exhibits a superior performance in the case of coarse distorted meshes. It can be useful for the 3D stress analysis of thin and thick metal/ceramic plates because the SaS formulation gives an opportunity to obtain the solutions with a prescribed accuracy, which asymptotically approach the 3D exact solutions of elasticity as the number of SaS tends to infinity.

ARTICLE HISTORY

Received 15 March 2016
Accepted 04 May 2016

KEYWORDS

Hybrid-mixed ANS quadrilateral element; functionally graded material plate; 3D stress analysis; sampling surfaces concept

1. Introduction

Functionally graded (FG) materials are a new class of advanced materials in which the material properties vary continuously from point to point. This property is achieved by varying the volume fraction of constituents. One of the advantages of the monotonic variation of the volume fraction of constituent phases is the elimination of stress discontinuity that is often encountered in laminated composites. The FG materials are usually made by mixing the metal and ceramic phases. The ceramic with the low thermal conductivity serves as a thermal barrier and is placed at high-temperature locations, whereas the metal is placed at regions where the mechanical properties such as toughness need to be high. The concept of the FG material was proposed by Japanese material scientists in the 1980s, and this is a subject of discussion in survey articles [1, 2]. However, most of the publications in the open literature appeared in the last fifteen years. The progress in the analytical and numerical modeling and analysis of FG materials and structures is reviewed in [3–5].

Nowadays, the finite element method (FEM) is widely used in bending, buckling and vibration analyses of FG plates and shells because of its advantages compared with other numerical techniques. The finite element formulations for the FG plates were developed in [6–11] through the first-order shear deformation theory (FSDT), also known as a Mindlin plate theory. Praveen and Reddy [6] considered a four-node rectangular plate element with five degrees of freedom (DOFs) per node to analyze the

thermoelastic response of FG plates. The major problem in constructing the low-order triangular and quadrilateral plate elements is how to eliminate shear locking for thin plates. To solve such problem, a simple locking-free discontinuous Galerkin triangular element of nonconforming type can be utilized, taking the piecewise linear nonconforming approximation for the rotations and transverse displacement [8]. The triangular plate elements with a node-based strain smoothing have been developed in [9]. The shear locking phenomenon is efficiently cured by a discrete shear gap technique. The nodal integrated finite element formulation is presented in [10]. The proposed triangular and quadrilateral plate elements are free of locking and show little sensitivity to geometric distortions. The isogeometric FEM based on nonuniform rational B-splines (NURBS) has been considered in [11]. It was established that shear locking can be overcome employing the NURBS functions of high order.

El-Abbasi and Meguid [12] presented a four-node shell element within the framework of FSDT accounting for thickness stretching for the analysis of FG plates and shells. For this purpose, they extended the isoparametric four-node finite element based on the 7-parameter shell formulation [13] that makes it possible to circumvent thickness locking. To avoid shear locking, the assumed natural strain (ANS) concept is employed. Arciniega and Reddy [14] developed the exact geometry or *geometrically exact* (GeX) shell elements on the basis of the 7-parameter formulation. The term “GeX” reflects the fact that the parametrization of the reference surface is known a priori and,

therefore, the coefficients of the first and second fundamental forms of its surface can be taken exactly at each element node. The regular meshes of high-order finite elements with seven DOFs per node are utilized. By increasing the p-level of the finite element approximation within each element, they eliminated shear locking and membrane locking because the exact representation of the reference surface yields the explicit variation of curvatures and Christoffel symbols throughout the low-order GeX shell elements.

The finite element models for the static and dynamic analyses of FG plates and shells were developed in [15–21] through the higher-order shear deformation theory (HSDT). Reddy [15] proposed rectangular plate elements by using Lagrangian and Hermitian interpolation functions to describe the in-plane displacements, rotations and transverse displacement, respectively. The shear locking phenomenon is avoided by means of the reduced integration throughout the element. A three-node triangular plate element with global and local displacement components for the analysis of laminated plates with an embedded FG layer has been built by Zhen and Wanji [16]. It is assumed that the global displacement components correspond to Reddy's HSDT [15]. The most attractive feature of the global-local approach is that the boundary conditions on bottom and top surfaces and the continuity conditions at interfaces for the transverse shear stresses are satisfied without employing postprocessing procedures. The isogeometric finite element formulation based on NURBS functions is discussed in [21]. Because of the smoothness of NURBS, it is possible to fulfill the C^1 -continuity requirement of Reddy's HSDT that is achieved by choosing at least the quadratic interpolation with no repeated knot vector entries.

More general finite element formulations on the basis of HSDT accounting for the transverse normal deformation for bending, buckling and free vibration analyses of FG plates and shells can be found in [22–24]. Talha and Singh [22] developed a nine-node rectangular plate element with 13 DOFs per node instead of 11 basic DOFs used in their HSDT in order to construct the C^0 -continuous finite element. The NURBS-based FEM for FG isotropic and sandwich plates has been proposed in [23]. The feature of this approach is that only four displacement DOFs are utilized. The C^1 -continuity requirement, however, can be easily carried out with the help of NURBS functions, and no shear locking occurs. An efficient nine-node rectangular FG shell element with 15 DOFs per node [24] has been developed via Carrera's unified formulation [25, 26]. The shear and membrane-locking phenomena are prevented through the ANS method. Note that all finite elements considered do not describe well the through-thickness distribution of transverse stresses, except for [24] where the fourth-order theory was utilized. However, the authors [24] report that the transverse normal stress is calculated with a large error in the case of thin plates because of the small value of this stress compared to in-plane stresses.

The present paper is intended to overcome the above mentioned difficulties and develop the finite element that makes it possible to evaluate all stress components effectively for the thick and very thin FG plates. To solve such a problem, the four-node quadrilateral plate element using the method of sampling surfaces (SaS) [27, 28] is proposed. The SaS formulation is based

on choosing inside the plate body N not equally spaced surfaces $\Omega^1, \Omega^2, \dots, \Omega^N$ parallel to the middle surface in order to introduce the displacement vectors $\mathbf{u}^1, \mathbf{u}^2, \dots, \mathbf{u}^N$ of these surfaces as basic plate variables, where $N \geq 3$. Such choice of unknowns with the consequent use of Lagrange polynomials of degree $N - 1$ in the assumed distributions of displacements, strains and mechanical properties through the thickness allows the presentation of governing equations of the SaS formulation in a very compact form. Recently, the SaS formulation was utilized to evaluate analytically the 3D stress state in FG plates and shells [29–34].

It should be noted that the SaS formulation with equally spaced SaS does not work properly with the Lagrange polynomials of high degree because of the Runge's phenomenon [35]. This phenomenon can yield the wild oscillation at the edges of the interval when the user deals with any specific functions. If the number of equispaced nodes is increased, then the oscillations become even larger. However, the use of the Chebyshev polynomial nodes [36] inside the plate body can help to improve significantly the behavior of the Lagrange polynomials of high degree because such a choice permits one to minimize *uniformly* the error due to the Lagrange interpolation. This fact gives an opportunity to derive displacements and stresses with a prescribed accuracy employing the sufficient number of SaS. It means in turn that the numerical solutions based on the SaS technique *asymptotically* approach the exact solutions of elasticity as the number of SaS $N \rightarrow \infty$.

It is well established that the isoparametric low-order plate elements are sensitive to shear locking. To avoid shear locking and have no spurious zero-energy modes, the ANS method can be employed. According to this method, the constant-linear interpolations for assumed transverse shear strains are utilized to represent the pure bending deformations with no parasitic transverse shear strains. The ANS concept has been developed for the isoparametric plate elements in [37–39] (see also the text books [40, 41]) and provides an excellent performance in the case of distorted meshes.

To improve the computational efficiency of ANS low-order plate elements, a hybrid-mixed FEM can be applied. This method pioneered by Pian [42] is based on the robust interpolation of displacements on the element boundary to provide displacement compatibility between elements, whereas the internal stresses are assumed so as to satisfy the differential equilibrium equations. The Pian's hybrid stress finite element was originally based upon the principle of the stationary complementary energy. Alternatively, the assumed stress finite element was proposed by applying the Hellinger–Reissner variational principle that simplifies the evaluation of the element stiffness matrix [43, 44]. Then, the assumed strain [45, 46] and the assumed stress-strain [47, 48] finite elements were developed. The former is based on the modified Hellinger–Reissner functional in which displacements and strains are utilized as basic plate variables, whereas the latter departs from the Hu–Washizu functional depending on displacements, strains and stresses. Here, following Pian we use the term “hybrid-mixed finite element” that covers all finite elements, which are “formulated by multivariable variational functional, yet the resulting matrix equations consist of only the nodal values of displacements as unknowns” [49].

In a proposed hybrid-mixed four-node quadrilateral element formulation, all SaS are located at Chebyshev polynomial nodes that make it possible to use the Lagrange polynomials of high degree. To avoid shear locking and have no spurious zero-energy modes in the case of distorted meshes, the assumed interpolations of displacement-independent strains and stress resultants in conjunction with the ANS interpolation of displacement-dependent transverse shear strains are utilized. To solve this problem, the Hu-Washizu multivariable variational principle is invoked. The developed isoparametric hybrid-mixed stress-strain element for the 3D stress analysis of FG plates has computational advantages compared to the hybrid-mixed strain and hybrid-mixed stress finite elements. This is due to the fact that here no expensive numerical inversion of elemental matrices is needed; all matrix inversions can be done analytically. On the contrary, in a conventional hybrid-mixed FEM [43–46] the inversion of the flexibility matrix is required. In fact, it is the most costly operation because the number of stress or strain parameters (modes) to be introduced to analyze effectively the FG composite plates can be sufficiently large [50]. Note also that the proposed hybrid-mixed finite element model generalizes authors' displacement-based finite element models for the stress analysis of plates and shells with equispaced SaS [51, 52] and the hybrid-mixed quadrilateral four-node element model for homogeneous plates with the SaS located at Chebyshev polynomial nodes [53].

2. Three-dimensional description of FG plates

Consider an FG plate of the thickness h . The plate can be defined as a 3D body of volume V bounded by two outer surfaces Ω^- , Ω^+ and the edge surface Σ . Let the middle surface Ω be described by Cartesian coordinates x^1 and x^2 , whereas the coordinate x^3 is oriented in the thickness direction (Figure 1). Introduce inside the plate body N not equally spaced SaS Ω^I parallel to the middle surface in order to introduce the displacements of these surfaces as basic plate variables. The transverse coordinates of SaS are defined as:

$$z^I = -\frac{h}{2} \cos\left(\pi \frac{2I-1}{2N}\right), \quad (1)$$

where $I = 1, 2, \dots, N$.

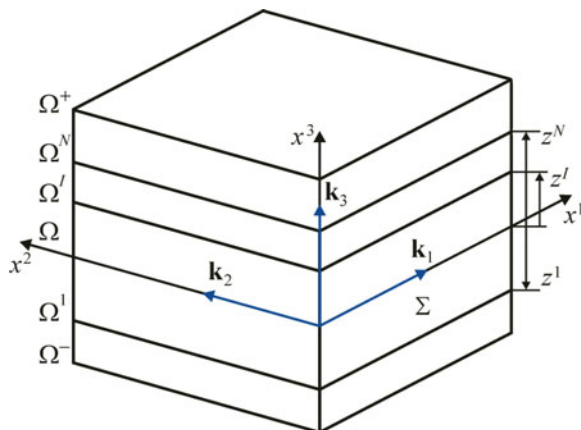


Figure 1. Geometry of the plate.

It is worth noting that the transverse coordinates of SaS (1) coincide with the coordinates of Chebyshev polynomial nodes [36]. This fact has a great meaning for a convergence of the SaS method as proved analytically in [28, 54].

The strain tensor is given by:

$$2\varepsilon_{ij} = u_{i,j} + u_{j,i}, \quad (2)$$

where u_i are the displacements. Here and in the following developments, Latin indices i, j, k, l range from 1 to 3, whereas Greek indices α, β range from 1 to 2.

Let us introduce displacements of SaS $u_i^I(x^1, x^2)$ as basic plate unknowns:

$$u_i^I = u_i(z^I). \quad (3)$$

Using the displacements (3), we can define strains of SaS $\varepsilon_{ij}^I(x^1, x^2)$ as:

$$\begin{aligned} 2\varepsilon_{\alpha\beta}^I &= 2\varepsilon_{\alpha\beta}(z^I) = u_{\alpha,\beta}^I + u_{\beta,\alpha}^I, \\ 2\varepsilon_{\alpha 3}^I &= 2\varepsilon_{\alpha 3}(z^I) = \beta_{\alpha}^I + u_{3,\alpha}^I, \\ \varepsilon_{33}^I &= \varepsilon_{33}(z^I) = \beta_3^I, \end{aligned} \quad (4)$$

where $\beta_i^I(x^1, x^2)$ are the derivatives of displacements with respect to the thickness coordinate at SaS defined as:

$$\beta_i^I = u_{i,3}(z^I). \quad (5)$$

3. Displacement and strain distributions in thickness direction

Up to this moment, no assumptions concerning the displacement field have been made. We start now with the first assumption of the proposed higher-order plate formulation. Let us assume that the displacements are distributed through the thickness in the following form:

$$u_i = \sum_I L^I u_i^I, \quad (6)$$

where $L^I(x^3)$ are the Lagrange polynomials of degree $N-1$ given by:

$$L^I = \prod_{J \neq I} \frac{x^3 - z^J}{z^I - z^J}. \quad (7)$$

The use of Eqs. (5)–(7) yields:

$$\beta_i^I = \sum_J M^J(z^I) u_i^J, \quad (8)$$

where $M^I = L_{,3}^I$ are the polynomials of degree $N-2$; their values on SaS can be expressed as:

$$\begin{aligned} M^J(z^I) &= \frac{1}{z^I - z^I} \prod_{K \neq I, J} \frac{z^I - z^K}{z^I - z^K} \quad (J \neq I), \\ M^I(z^I) &= -\sum_{J \neq I} M^J(z^I), \end{aligned} \quad (9)$$

where $I, J, K = 1, 2, \dots, N$. Thus, the key functions β_i^I of the proposed higher-order plate formulation are represented

according to Eq. (8) as a linear combination of displacements of SaS u_i^l .

Proposition 1. The functions $\beta_i^1, \beta_i^2, \dots, \beta_i^N$ are linearly dependent, that is there exist numbers $\alpha^1, \alpha^2, \dots, \alpha^N$, which are not all zero, such that:

$$\alpha^T \beta_i = 0, \tag{10}$$

$$\alpha = [\alpha^1 \ \alpha^2 \ \dots \ \alpha^N]^T, \quad \beta_i = [\beta_i^1 \ \beta_i^2 \ \dots \ \beta_i^N]^T. \tag{11}$$

The proof of this proposition follows from a homogeneous system of linear equations:

$$\mathbf{M}^T \alpha = 0, \tag{12}$$

$$\mathbf{M} = \begin{bmatrix} M^1(z^1) & M^2(z^1) & \dots & M^N(z^1) \\ M^1(z^2) & M^2(z^2) & \dots & M^N(z^2) \\ \dots & \dots & \dots & \dots \\ M^1(z^N) & M^2(z^N) & \dots & M^N(z^N) \end{bmatrix}, \tag{13}$$

which has a nontrivial solution. This is due to the fact that \mathbf{M} is a singular matrix that follows directly from the identity:

$$\sum_I M^I(x^3) = 0. \tag{14}$$

The details of the proof can be found in [53].

The following step consists in a choice of the consistent approximation of strains through the thickness of the plate. It is apparent that the strain distribution should be chosen similar to the displacement distribution (6), that is,

$$\varepsilon_{ij} = \sum_I L^I \varepsilon_{ij}^I. \tag{15}$$

4. Hu-Washizu mixed variational formulation

To develop the hybrid-mixed stress-strain finite element formulation, we have to invoke the Hu-Washizu variational principal in which displacements, strains and stresses are utilized as independent variables [55]. It can be written as:

$$\delta J_{HW} = 0, \tag{16}$$

$$J_{HW} = \iint_{\Omega} \int_{-h/2}^{h/2} \left[\frac{1}{2} e_{ij} C_{ijkl} e_{kl} - \sigma_{ij} (e_{ij} - \varepsilon_{ij}) \right] dx^1 dx^2 dx^3 - \iint_{\Omega} (p_i^+ u_i^+ - p_i^- u_i^-) dx^1 dx^2 - W_{\Sigma}, \tag{17}$$

where σ_{ij} are the stresses, e_{ij} are the displacement-independent strains, C_{ijkl} are the components of the material tensor, u_i^- and u_i^+ are the displacements of bottom and top surfaces Ω^- and Ω^+ , p_i^- and p_i^+ are the tractions acting on the bottom and top surfaces, W_{Σ} is the work done by external loads applied to the edge surface Σ . Here and in the following developments, the summation on repeated Latin indices is implied.

Following the SaS technique, we introduce the third assumption of the proposed hybrid-mixed plate formulation. Assume that the displacement-independent strains are

distributed through the thickness similar to displacement-dependent strains (15):

$$e_{ij} = \sum_I L^I e_{ij}^I, \tag{18}$$

where $e_{ij}^I(x^1, x^2)$ are the displacement-independent strains of SaS.

Next, we accept the last assumption of the SaS FG plate formulation [29, 32]. Let the material constants be distributed through the thickness of a plate as follows:

$$C_{ijkl} = \sum_I L^I C_{ijkl}^I, \tag{19}$$

where $C_{ijkl}^I = C_{ijkl}^I(z^I)$ are the values of material constants on SaS.

Substituting the through-thickness distributions of strains and material properties (15), (18) and (19) in the functional (17) and introducing stress resultants:

$$H_{ij}^I = \int_{-h/2}^{h/2} \sigma_{ij} L^I dx^3, \tag{20}$$

the following variational equation is obtained:

$$\begin{aligned} & \iint_{\Omega} \sum_I \left[\delta(\mathbf{e}^I)^T \left(\mathbf{H}^I - \sum_{J,K} \Lambda^{JK} \mathbf{C}^J \mathbf{e}^K \right) \right. \\ & \left. + \delta(\mathbf{H}^I)^T (\mathbf{e}^I - \boldsymbol{\varepsilon}^I) - \delta(\mathbf{e}^I)^T \mathbf{H}^I \right] dx^1 dx^2 \\ & + \iint_{\Omega} (p_i^+ \delta u_i^+ - p_i^- \delta u_i^-) dx^1 dx^2 + \delta W_{\Sigma} = 0, \end{aligned} \tag{21}$$

where

$$\begin{aligned} \mathbf{e}^I &= [\varepsilon_{11}^I \ \varepsilon_{22}^I \ \varepsilon_{33}^I \ 2\varepsilon_{12}^I \ 2\varepsilon_{13}^I \ 2\varepsilon_{23}^I]^T, \\ \boldsymbol{\varepsilon}^I &= [e_{11}^I \ e_{22}^I \ e_{33}^I \ 2e_{12}^I \ 2e_{13}^I \ 2e_{23}^I]^T, \\ \mathbf{H}^I &= [H_{11}^I \ H_{22}^I \ H_{33}^I \ H_{12}^I \ H_{13}^I \ H_{23}^I]^T, \\ \mathbf{C}^I &= \begin{bmatrix} C_{1111}^I & C_{1122}^I & C_{1133}^I & C_{1112}^I & 0 & 0 \\ C_{2211}^I & C_{2222}^I & C_{2233}^I & C_{2212}^I & 0 & 0 \\ C_{3311}^I & C_{3322}^I & C_{3333}^I & C_{3312}^I & 0 & 0 \\ C_{1211}^I & C_{1222}^I & C_{1233}^I & C_{1212}^I & 0 & 0 \\ 0 & 0 & 0 & 0 & C_{1313}^I & C_{1323}^I \\ 0 & 0 & 0 & 0 & C_{2313}^I & C_{2323}^I \end{bmatrix}, \\ \Lambda^{JK} &= \int_{-h/2}^{h/2} L^J L^K dx^3. \end{aligned} \tag{22}$$

5. Hybrid-mixed ANS finite element formulation

In the isoparametric four-node quadrilateral plate element formulation, the position vector and the displacement vector are

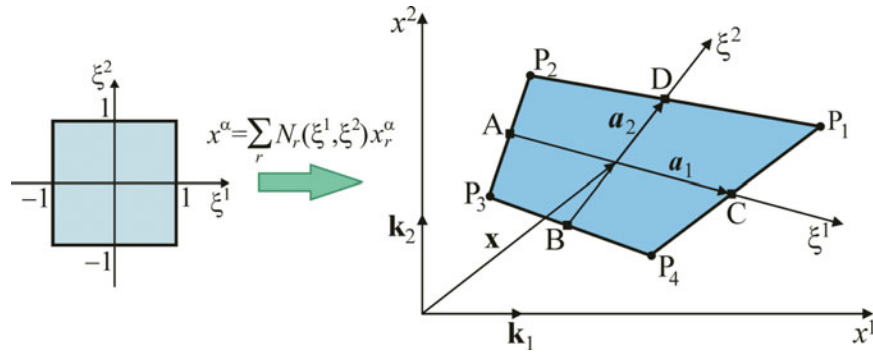


Figure 2. Quadrilateral plate element.

approximated according to the standard C^0 interpolation:

$$x^\alpha = \sum_r N_r x_r^\alpha, \quad (23)$$

$$u_i^I = \sum_r N_r u_{ir}^I, \quad (24)$$

$$N_r = \frac{1}{4} (1 + n_{1r} \xi^1) (1 + n_{2r} \xi^2), \quad (25)$$

where $N_r(\xi^1, \xi^2)$ are the bilinear shape functions of the finite element with $n_{11} = n_{14} = n_{21} = n_{22} = 1$ and $n_{12} = n_{13} = n_{23} = n_{24} = -1$, x_r^α are the nodal coordinates, u_{ir}^I are the displacements of SaS at element nodes, the index r denotes the number of nodes and ranges from 1 to 4. The surface traction vector is also assumed to vary bilinearly throughout the element. The local numbering of the corner nodes and middle side nodes is shown in Figure 2.

To overcome shear locking and have no spurious zero-energy modes, the robust ANS interpolation [37, 39] of transverse shear strains of SaS with four sampling points can be utilized:

$$\varepsilon_{\alpha 3}^I = \ell_\alpha^\beta \hat{\varepsilon}_{\beta 3}^I, \quad (26)$$

$$\hat{\varepsilon}_{13}^I = \frac{1}{2} (1 - \xi^2) \hat{\varepsilon}_{13}^I(B) + \frac{1}{2} (1 + \xi^2) \hat{\varepsilon}_{13}^I(D),$$

$$\hat{\varepsilon}_{23}^I = \frac{1}{2} (1 - \xi^1) \hat{\varepsilon}_{23}^I(A) + \frac{1}{2} (1 + \xi^1) \hat{\varepsilon}_{23}^I(C), \quad (27)$$

where $\hat{\varepsilon}_{\alpha 3}^I$ are the covariant components of the strain tensor at SaS in the contravariant basis \mathbf{a}^i , which are defined by the orthogonality condition $\mathbf{a}_i \cdot \mathbf{a}^j = \delta_i^j$:

$$\mathbf{a}_\alpha = t_\alpha^\beta \mathbf{k}_\beta, \quad \mathbf{a}^\alpha = \ell_\beta^\alpha \mathbf{k}^\beta, \quad \mathbf{a}_3 = \mathbf{a}^3 = \mathbf{k}_3,$$

$$t_\alpha^\beta = \frac{\partial x^\beta}{\partial \xi^\alpha}, \quad \ell_\alpha^\beta = \frac{\partial \xi^\beta}{\partial x^\alpha},$$

$$t_1^\alpha = \frac{1}{4} (1 + \xi^2) (x_1^\alpha - x_2^\alpha) + \frac{1}{4} (1 - \xi^2) (x_4^\alpha - x_3^\alpha),$$

$$t_2^\alpha = \frac{1}{4} (1 + \xi^1) (x_1^\alpha - x_4^\alpha) + \frac{1}{4} (1 - \xi^1) (x_2^\alpha - x_3^\alpha),$$

$$\ell_1^1 = \frac{1}{\Delta} t_2^2, \quad \ell_1^2 = -\frac{1}{\Delta} t_2^1, \quad \ell_2^1 = -\frac{1}{\Delta} t_1^2, \quad \ell_2^2 = \frac{1}{\Delta} t_1^1, \quad (28)$$

where $\Delta = \det \mathbf{J}$ is the determinant of the Jacobian matrix $\mathbf{J} = [t_\alpha^\beta]$, whereas $\mathbf{J}^{-1} = [\ell_\alpha^\beta]$ stands for the inverse Jacobian matrix. The transverse shear strains $\hat{\varepsilon}_{\alpha 3}^I$ at sampling points A, B, C and D are evaluated according to Eqs. (4) and (8) as:

$$2\hat{\varepsilon}_{13}^I(B) = \frac{1}{2} (u_{34}^I - u_{33}^I) + \frac{1}{4} \sum_J M^J(z^J) (x_4^\alpha - x_3^\alpha) (u_{\alpha 3}^I + u_{\alpha 4}^I),$$

$$2\hat{\varepsilon}_{13}^I(D) = \frac{1}{2} (u_{31}^I - u_{32}^I) + \frac{1}{4} \sum_J M^J(z^J) (x_1^\alpha - x_2^\alpha) (u_{\alpha 1}^I + u_{\alpha 2}^I),$$

$$2\hat{\varepsilon}_{23}^I(A) = \frac{1}{2} (u_{32}^I - u_{33}^I) + \frac{1}{4} \sum_J M^J(z^J) (x_2^\alpha - x_3^\alpha) (u_{\alpha 2}^I + u_{\alpha 3}^I),$$

$$2\hat{\varepsilon}_{23}^I(C) = \frac{1}{2} (u_{31}^I - u_{34}^I) + \frac{1}{4} \sum_J M^J(z^J) (x_1^\alpha - x_4^\alpha) (u_{\alpha 1}^I + u_{\alpha 4}^I). \quad (29)$$

Substituting the approximation (24) in Eqs. (4) and (8), using a formula for derivatives of the shape functions:

$$\begin{bmatrix} \frac{\partial N_r}{\partial x^1} \\ \frac{\partial N_r}{\partial x^2} \end{bmatrix} = \mathbf{J}^{-1} \begin{bmatrix} \frac{\partial N_r}{\partial \xi^1} \\ \frac{\partial N_r}{\partial \xi^2} \end{bmatrix} \quad (30)$$

and accounting for Eqs. (26), (27) and (29), one obtains:

$$\boldsymbol{\varepsilon}^I = \mathbf{B}^I \mathbf{U}, \quad (31)$$

$$\mathbf{U} = [\mathbf{U}_1^T \mathbf{U}_2^T \mathbf{U}_3^T \mathbf{U}_4^T]^T,$$

$$\mathbf{U}_r = [u_{1r}^1 \ u_{2r}^1 \ u_{3r}^1 \ u_{1r}^2 \ u_{2r}^2 \ u_{3r}^2 \ \dots \ u_{1r}^N \ u_{2r}^N \ u_{3r}^N]^T, \quad (32)$$

where \mathbf{U}_r are the nodal displacement vectors of the element, $\mathbf{B}^I(\xi^1, \xi^2)$ are the strain-displacement transformation matrices of order $6 \times 12N$ related to SaS.

To improve the computational efficiency of the ANS four-node quadrilateral plate element, a hybrid-mixed method may be employed. In order to fulfill the patch test [43], the assumed stress resultants are interpolated throughout the element as follows:

$$\mathbf{H}^I = \mathbf{P}_\sigma \boldsymbol{\Phi}^I, \quad \boldsymbol{\Phi}^I = [\Phi_1^I \ \Phi_2^I \ \dots \ \Phi_{12}^I]^T, \quad (33)$$

$$\mathbf{P}_\sigma = \begin{bmatrix} 1 & 0 & 0 & 0 & 0 & 0 & \bar{t}_1^1 \bar{t}_1^1 \bar{\xi}^2 & \bar{t}_2^1 \bar{t}_2^1 \bar{\xi}^1 & 0 & 0 & 0 & 0 \\ 0 & 1 & 0 & 0 & 0 & 0 & \bar{t}_1^2 \bar{t}_1^2 \bar{\xi}^2 & \bar{t}_2^2 \bar{t}_2^2 \bar{\xi}^1 & 0 & 0 & 0 & 0 \\ 0 & 0 & 1 & 0 & 0 & 0 & 0 & 0 & \bar{\xi}^1 & \bar{\xi}^2 & 0 & 0 \\ 0 & 0 & 0 & 1 & 0 & 0 & \bar{t}_1^1 \bar{t}_1^2 \bar{\xi}^2 & \bar{t}_2^1 \bar{t}_2^2 \bar{\xi}^1 & 0 & 0 & 0 & 0 \\ 0 & 0 & 0 & 0 & 1 & 0 & 0 & 0 & 0 & 0 & \bar{t}_1^1 \bar{\xi}^2 & \bar{t}_2^1 \bar{\xi}^1 \\ 0 & 0 & 0 & 0 & 0 & 1 & 0 & 0 & 0 & 0 & \bar{t}_1^2 \bar{\xi}^2 & \bar{t}_2^2 \bar{\xi}^1 \end{bmatrix}, \tag{34}$$

where \bar{t}_α^β are the elements of the Jacobian matrix (28) evaluated at the element center, and $\bar{\xi}^\alpha$ are the transformed coordinates defined as:

$$\begin{aligned} \bar{t}_1^\alpha &= \frac{1}{4} (x_1^\alpha - x_2^\alpha - x_3^\alpha + x_4^\alpha), & \bar{t}_2^\alpha &= \frac{1}{4} (x_1^\alpha + x_2^\alpha - x_3^\alpha - x_4^\alpha), \\ \bar{\xi}^\alpha &= \xi^\alpha - \xi_c^\alpha, & \xi_c^\alpha &= \frac{1}{A_{el}} \int_{-1}^1 \int_{-1}^1 \xi^\alpha \Delta d\xi^1 d\xi^2, \\ A_{el} &= \int_{-1}^1 \int_{-1}^1 \Delta d\xi^1 d\xi^2, \\ \Delta &= c_0 + c_1 \xi^1 + c_2 \xi^2, \\ c_0 &= \frac{1}{8} [(x_1^1 - x_3^1) (x_2^2 - x_4^2) - (x_2^1 - x_4^1) (x_1^2 - x_3^2)], \\ c_1 &= \frac{1}{8} [(x_1^1 - x_2^1) (x_3^2 - x_4^2) - (x_3^1 - x_4^1) (x_1^2 - x_2^2)], \\ c_2 &= \frac{1}{8} [(x_1^1 - x_4^1) (x_2^2 - x_3^2) - (x_2^1 - x_3^1) (x_1^2 - x_4^2)]. \end{aligned} \tag{35}$$

The purpose of introducing $\bar{\xi}^\alpha$ lies in the simplicity of some elemental matrices of the hybrid-mixed method [56, 57] because a useful formula

$$\int_{-1}^1 \int_{-1}^1 \bar{\xi}^\alpha \Delta d\xi^1 d\xi^2 = 0 \tag{36}$$

holds.

The displacement-independent strains of SaS are interpolated throughout the element following [58, 59] as:

$$\mathbf{e}^I = \mathbf{P}_e \boldsymbol{\Psi}^I, \quad \boldsymbol{\Psi}^I = [\Psi_1^I \ \Psi_2^I \ \dots \ \Psi_{12}^I]^T, \tag{37}$$

$$\mathbf{P}_e = \begin{bmatrix} 1 & 0 & 0 & 0 & 0 & 0 & \bar{\ell}_1^1 \bar{\ell}_1^1 \bar{\xi}^2 & \bar{\ell}_2^1 \bar{\ell}_2^1 \bar{\xi}^1 & 0 & 0 & 0 & 0 \\ 0 & 1 & 0 & 0 & 0 & 0 & \bar{\ell}_1^2 \bar{\ell}_1^2 \bar{\xi}^2 & \bar{\ell}_2^2 \bar{\ell}_2^2 \bar{\xi}^1 & 0 & 0 & 0 & 0 \\ 0 & 0 & 1 & 0 & 0 & 0 & 0 & 0 & \bar{\xi}^1 & \bar{\xi}^2 & 0 & 0 \\ 0 & 0 & 0 & 1 & 0 & 0 & 2\bar{\ell}_1^1 \bar{\ell}_2^1 \bar{\xi}^2 & 2\bar{\ell}_1^2 \bar{\ell}_2^2 \bar{\xi}^1 & 0 & 0 & 0 & 0 \\ 0 & 0 & 0 & 0 & 1 & 0 & 0 & 0 & 0 & 0 & \bar{\ell}_1^1 \bar{\xi}^2 & \bar{\ell}_2^1 \bar{\xi}^1 \\ 0 & 0 & 0 & 0 & 0 & 1 & 0 & 0 & 0 & 0 & \bar{\ell}_2^1 \bar{\xi}^2 & \bar{\ell}_2^2 \bar{\xi}^1 \end{bmatrix} \tag{38}$$

that corresponds to the interpolation of stress resultants (33) and (34), where $\bar{\ell}_\alpha^\beta$ are the elements of the inverse Jacobian matrix evaluated at the element center:

$$\bar{\ell}_1^1 = \frac{1}{c_0} \bar{t}_2^2, \quad \bar{\ell}_1^2 = -\frac{1}{c_0} \bar{t}_1^2, \quad \bar{\ell}_2^1 = -\frac{1}{c_0} \bar{t}_1^1, \quad \bar{\ell}_2^2 = \frac{1}{c_0} \bar{t}_2^1. \tag{39}$$

Substituting interpolations (24), (31), (33) and (37) in the Hu-Washizu variational Eq. (21) and taking into account relations:

$$u_i^+ = \sum_I L^I(h/2)u_i^I, \quad u_i^- = \sum_I L^I(-h/2)u_i^I, \tag{40}$$

we arrive at the element equilibrium equations:

$$\mathbf{Q}^T \boldsymbol{\Phi}^I = \sum_{J,K} \Lambda^{JK} \mathbf{D}^J \boldsymbol{\Psi}^K, \tag{41}$$

$$\mathbf{Q} \boldsymbol{\Psi}^I = \mathbf{R}^I \mathbf{U}, \tag{42}$$

$$\sum_I (\mathbf{R}^I)^T \boldsymbol{\Phi}^I = \mathbf{F}, \tag{43}$$

where \mathbf{F} is the element-wise surface traction vector; \mathbf{Q} , \mathbf{D}^J and \mathbf{R}^I are the elemental matrices given by:

$$\mathbf{Q} = \int_{-1}^1 \int_{-1}^1 \mathbf{P}_\sigma^T \mathbf{P}_e \Delta d\xi^1 d\xi^2, \tag{44}$$

$$\mathbf{D}^J = \int_{-1}^1 \int_{-1}^1 \mathbf{P}_e^T \mathbf{C}^J \mathbf{P}_e \Delta d\xi^1 d\xi^2,$$

$$\mathbf{R}^I = \int_{-1}^1 \int_{-1}^1 \mathbf{P}_\sigma^T \mathbf{B}^I \Delta d\xi^1 d\xi^2. \tag{45}$$

The use of transformed coordinates $\bar{\xi}^\alpha$ in interpolations (33) and (37) is of great importance because the flexibility matrix becomes quasi-diagonal, that is,

$$\mathbf{Q} = A_{el} \text{diag} \left(\mathbf{I}_6, \ \omega_{22}, \ \omega_{11}, \ \begin{bmatrix} \omega_{11} & \omega_{12} \\ \omega_{12} & \omega_{22} \end{bmatrix}, \ \omega_{22}, \ \omega_{11} \right), \tag{46}$$

where \mathbf{I}_6 is the unit matrix of order 6×6 and

$$\begin{aligned} A_{el} &= 4c_0, & \omega_{\alpha\beta} &= \frac{1}{A_{el}} \int_{-1}^1 \int_{-1}^1 \bar{\xi}^\alpha \bar{\xi}^\beta \Delta d\xi^1 d\xi^2 \\ & & &= \frac{1}{3} \left(\delta_{\alpha\beta} - \frac{c_\alpha c_\beta}{3c_0 c_0} \right). \end{aligned} \tag{47}$$

Owing to interpolations (33) and (37), the stress resultants and displacement-independent strains of SaS are discontinuous at the element boundaries. Hence, the column matrices Φ^I and Ψ^I can be eliminated on the element level that yields finite element equations:

$$\mathbf{K}\mathbf{U} = \mathbf{F}, \quad (48)$$

where \mathbf{K} is the element stiffness matrix of order $12N \times 12N$ defined as:

$$\mathbf{K} = \sum_{I, J, K} \Lambda^{IJK} (\mathbf{R}^I)^T \mathbf{Q}^{-1} \mathbf{D}^J \mathbf{Q}^{-1} \mathbf{R}^K. \quad (49)$$

Since the matrix \mathbf{Q} is quasi-diagonal, its inversion can be easily fulfilled in a closed form:

$$\mathbf{Q}^{-1} = \frac{1}{A_{\text{el}}} \text{diag} \left(\mathbf{I}_6, 1/\omega_{22}, 1/\omega_{11}, \begin{bmatrix} \omega_{22}/d & -\omega_{12}/d \\ -\omega_{12}/d & \omega_{11}/d \end{bmatrix}, 1/\omega_{22}, 1/\omega_{11} \right), \quad (50)$$

where $d = \omega_{11}\omega_{22} - \omega_{12}\omega_{12}$. Thus, no expensive numerical inversion is needed if one uses the hybrid-mixed stress-strain quadrilateral plate element developed.

Proposition 2. There is a link between displacement-dependent and displacement-independent strains of SaS:

$$\int_{-1}^1 \int_{-1}^1 \mathbf{P}_\sigma^T (\mathbf{e}^I - \mathbf{e}^J) \Delta d\xi^1 d\xi^2 = 0. \quad (51)$$

This proposition can be proved simply considering the *orthogonality* condition, which follows directly from the variational Eq. (21),

$$\int_{-1}^1 \int_{-1}^1 \delta(\mathbf{H}^I)^T (\mathbf{e}^I - \mathbf{e}^J) \Delta d\xi^1 d\xi^2 = 0 \quad (52)$$

and the assumed interpolation of stress resultants (33). The orthogonality condition (51) will be employed below for assessment of the rank of the stiffness matrix (49).

Remark 1. As we remember, L^I are the Lagrange polynomials of degree $N - 1$. This makes it possible to carry out *exact* integration in (22) utilizing the n -point Gaussian quadrature rule, where $n = (3N - 2)/2$ for even N and $n = (3N - 1)/2$ for odd N . It should be mentioned also that the elemental matrices (45) are evaluated through the Gauss integration scheme with 2×2 sampling points.

Remark 2. The displacement-independent strains (37) are selected such that the four-node quadrilateral plate element would be free of shear locking and kinematically stable. It is apparent that the assumed strain interpolation should be chosen to be as simple as possible. Because of the strain interpolation (37), we introduced 12 assumed strain parameters $\Psi_1^I, \Psi_2^I, \dots, \Psi_{12}^I$ for each SaS, that is $12N$ for all SaS. It seems to be excessive recalling about $3N$ displacement DOFs per node. However, there exist six dependent strain modes exactly, which

provide a correct rank of the element stiffness matrix [53]:

$$\boldsymbol{\alpha}^T [\Psi_3^1 \ \Psi_3^2 \ \dots \ \Psi_3^N]^T = 0, \quad (53)$$

$$\boldsymbol{\alpha}^T [\Psi_9^1 \ \Psi_9^2 \ \dots \ \Psi_9^N]^T = 0, \quad (54)$$

$$\boldsymbol{\alpha}^T [\Psi_{10}^1 \ \Psi_{10}^2 \ \dots \ \Psi_{10}^N]^T = 0, \quad (55)$$

$$\boldsymbol{\alpha}^T [\Psi_{11}^1 \ \Psi_{11}^2 \ \dots \ \Psi_{11}^N]^T = \boldsymbol{\alpha}^T [\Psi_{12}^1 \ \Psi_{12}^2 \ \dots \ \Psi_{12}^N]^T, \quad (56)$$

$$2\boldsymbol{\lambda}^T \mathbf{M} [\Psi_5^1 \ \Psi_5^2 \ \dots \ \Psi_5^N]^T = \boldsymbol{\lambda}^T [\Psi_9^1 \ \Psi_9^2 \ \dots \ \Psi_9^N]^T, \quad (57)$$

$$2\boldsymbol{\lambda}^T \mathbf{M} [\Psi_6^1 \ \Psi_6^2 \ \dots \ \Psi_6^N]^T = \boldsymbol{\lambda}^T [\Psi_{10}^1 \ \Psi_{10}^2 \ \dots \ \Psi_{10}^N]^T, \quad (58)$$

where $\boldsymbol{\alpha} = [\alpha^1 \ \alpha^2 \ \dots \ \alpha^N]^T$ and $\boldsymbol{\lambda} = [\lambda^1 \ \lambda^2 \ \dots \ \lambda^N]^T$ are column matrices that exist owing to Propositions 1 and 2. Six coupling Eqs. (53)–(58) play a central role in the developed hybrid-mixed finite element formulation because they imply that only $12N - 6$ assumed strain modes are independent of $12N$ ones introduced by (37). Therefore, the element stiffness matrix has six zero eigenvalues as required for satisfaction of the general rigid-body motion representation.

6. Numerical examples

The performance of the proposed hybrid-mixed four-node FG plate element denoted by SaSQP4 element is evaluated with several finite element and exact solutions of elasticity including 3D patch tests.

6.1. Patch tests for an FG plate

The plate patch tests for the membrane behavior and out-of-plane bending behavior of quadrilateral elements confirm that the finite element formulation developed is able to reproduce the constant stress-strain states for distorted mesh configurations. Here, we consider a patch of five plate elements [60] with four external and four internal nodes as depicted in Figure 3.

It is assumed that the elastic modulus is distributed through the thickness according to the exponential law:

$$E = E^- e^{\alpha(z+0.5)}, \quad -0.5 \leq z \leq 0.5, \quad (59)$$

where E^- is the elastic modulus on the bottom surface, $z = x_3/h$ is the dimensionless thickness coordinate, α is the material gradient index defined as:

$$\alpha = \ln(E^+/E^-), \quad (60)$$

where E^+ is the elastic modulus on the top surface.

6.1.1. Membrane patch test

To achieve the constant membrane stress-strain state at surfaces parallel to the middle surface, the displacements of the FG plate can be taken as:

$$u_1 = e \left(x^1 + \frac{1}{2} x^2 \right), \quad u_2 = e \left(\frac{1}{2} x^1 + x^2 \right), \quad u_3 = 0. \quad (61)$$

Such displacement distribution leads to a constant in-plane strain field, that is,

$$\varepsilon_{11} = \varepsilon_{22} = e, \quad 2\varepsilon_{12} = e, \quad \varepsilon_{i3} = 0. \quad (62)$$

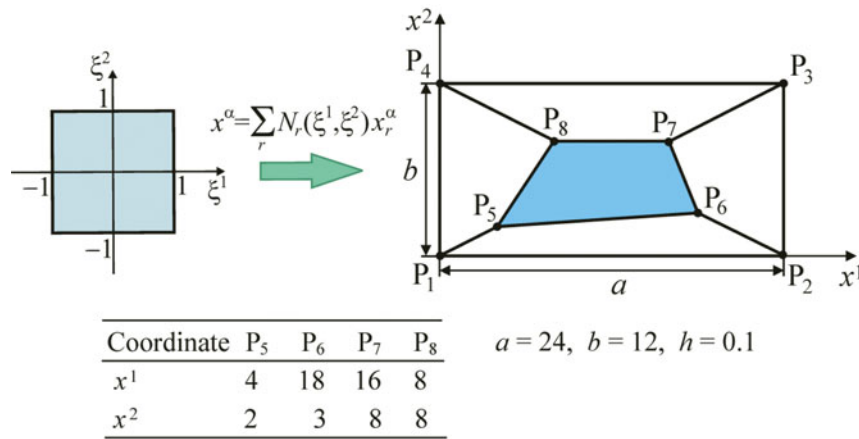


Figure 3. Patch test for an FG plate.

Note that in the case of zero Poisson’s ratios, both outer surfaces of the plate are free of transverse stresses.

Considering the solution (61), the displacements of SaS at exterior nodes can be prescribed as follows:

$$u_1^I = e \left(x^1 + \frac{1}{2}x^2 \right), \quad u_2^I = e \left(\frac{1}{2}x^1 + x^2 \right), \quad u_3^I = 0 \tag{63}$$

that yield

$$\varepsilon_{11}^I = \varepsilon_{22}^I = e, \quad 2\varepsilon_{12}^I = e, \quad \varepsilon_{i3}^I = 0. \tag{64}$$

As a numerical example, we consider an FG plate with $E^- = 10^6$, $\alpha = 2$ and $e = 10^{-5}$. The calculations show that the SaSQP4 element passes the membrane patch test for an FG plate. The maximum relative error for displacements of the top surface is reached at point P_7 for $N = 3$ and at point P_8 for $N = 7$ and is equal to 7.5×10^{-10} and 5.3×10^{-9} , correspondingly. It should be mentioned that the computations were performed on a standard PC employing the 16-digit calculation.

6.1.2. Bending patch test

To achieve the constant 3D bending stress-strain state, the displacements are chosen as:

$$u_1 = ex^3 \left(x^1 + \frac{1}{2}x^2 \right), \quad u_2 = ex^3 \left(\frac{1}{2}x^1 + x^2 \right), \tag{65}$$

$$u_3 = -\frac{1}{2}e [(x^1)^2 + x^1x^2 + (x^2)^2].$$

Substituting (65) in strain-displacement Eq. (2), we arrive at the constant strain state at surfaces parallel to the middle surface:

$$\varepsilon_{11} = \varepsilon_{22} = ex^3, \quad 2\varepsilon_{12} = ex^3, \quad \varepsilon_{i3} = 0. \tag{66}$$

Using (66) in constitutive equations, one can verify that the 3D equilibrium equations of an FG plate are fulfilled exactly for the zero Poisson’s ratio. Moreover, both outer surfaces of the plate will be free of surface tractions.

Taking into account (65), the displacements of SaS at exterior nodes are:

$$u_1^I = ez^I \left(x^1 + \frac{1}{2}x^2 \right), \quad u_2^I = ez^I \left(\frac{1}{2}x^1 + x^2 \right), \tag{67}$$

$$u_3^I = -\frac{1}{2}e [(x^1)^2 + x^1x^2 + (x^2)^2]$$

that result in

$$\varepsilon_{11}^I = \varepsilon_{22}^I = ez^I, \quad 2\varepsilon_{12}^I = ez^I, \quad \varepsilon_{i3}^I = 0. \tag{68}$$

Applying the prescribed displacements (67) to exterior nodes of the FG plate with $E^- = 10^6$, $\alpha = 2$ and $e = 10^{-5}$, one can observe that the displacements and strains at interior nodes are identical to analytical answers. This is partially confirmed by displacements of the top surface u_i^+ at interior nodes listed in Table 1 for three and seven SaS. Thus, the SaSQP4 element passes the bending patch test for the FG plate.

6.2. Cantilever FG trapezoidal plate

A trapezoidal plate is clamped on one side, whereas the opposite side is subjected to a distributed in-plane load [61], as shown in Figure 4. This test is an excellent ability to verify the proper representation of the membrane dominated stress state with skewed meshes. In the frame work of 2D elasticity, the cantilever

Table 1. Displacements at interior nodes in the bending patch test for an FG plate.

Formulation	Node	$10^6 \times u_1^+$	$10^6 \times u_2^+$	$-10^4 \times u_3^+$
Exact values	P ₅	2.5000000	2.0000000	1.4000000
	P ₆	9.7500000	6.0000000	19.350000
	P ₇	10.000000	8.0000000	22.400000
	P ₈	6.0000000	6.0000000	9.6000000
N = 3	P ₅	2.4999924	1.9999993	1.3999954
	P ₆	9.7500068	5.9999996	19.349998
	P ₇	10.000003	8.0000001	22.399997
	P ₈	5.9999974	6.0000007	9.5999966
N = 7	P ₅	2.4999924	1.9999993	1.3999954
	P ₆	9.7500068	5.9999982	19.349993
	P ₇	10.000010	8.0000009	22.399988
	P ₈	5.9999903	6.0000028	9.5999871

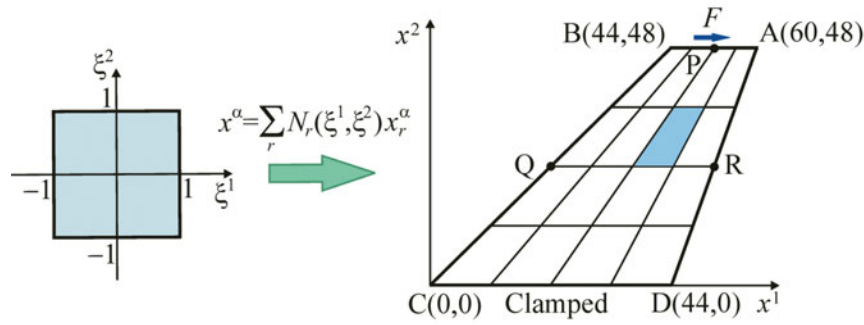


Figure 4. Cantilever trapezoidal plate.

Table 2. In-plane tip displacement u_1 at point P of the homogeneous trapezoidal plate.

Formulation	2 × 2	4 × 4	8 × 8	16 × 16	32 × 32	64 × 64	128 × 128
$N = 3$	16.70	21.21	23.03	23.64	23.85	23.92	23.96
$N = 5$	16.70	21.21	23.03	23.65	23.86	23.94	23.98
$N = 7$	16.70	21.21	23.03	23.65	23.86	23.95	23.99
Hueck [63]							23.96

Table 3. Maximum principal stress σ_{\max} at point Q and minimum principal stress σ_{\min} at point R of the homogeneous trapezoidal plate for $N = 5$.

Stress	4 × 4	8 × 8	16 × 16	32 × 32	64 × 64	128 × 128	Hueck [63]
$\sigma_{\max}(\text{Q})$	0.2239	0.2448	0.2445	0.2414	0.2393	0.2382	0.2369
$-\sigma_{\min}(\text{R})$	0.2161	0.2163	0.2120	0.2080	0.2059	0.2047	0.2035

trapezoidal plate has been investigated by many researchers (see, e.g., [61–63]).

First, we consider a homogeneous trapezoidal plate with $E = 1$, $\nu = 1/3$, $h = 1$ and $F = 1$. Table 2 lists the results of the convergence study due to increasing the number of SaS inside the plate body by using the in-plane tip displacement at point P belonging to the middle surface. A comparison with the results of Hueck and Wriggers [63] is also presented. As can be seen, the SaS formulation gives the possibility to calculate the displacements with four right digits by using not very large number of SaS. The results of the convergence study owing to mesh refinement utilizing the maximum principal stress at point Q and the minimum principal stress at point R with five SaS inside the plate are listed in Table 3. It is seen that the values of principal stresses are slightly larger than those reported in [63], where the authors restrict themselves to the plane stress problem. Herein, the finite element plate formulation in the framework of 3D elasticity is considered.

Then, we study an FG trapezoidal plate fabricated by mixing the metal and ceramic phases. For evaluating the effective material properties through the thickness of a two-phase plate, the

Mori–Tanaka method [64, 65] is adopted:

$$K = K_m + \frac{V_c(K_c - K_m)}{1 + V_m(K_c - K_m)/(K_m + 4G_m/3)},$$

$$G = G_m + \frac{V_c(G_c - G_m)}{1 + V_m(G_c - G_m)/(G_m + f_m)},$$

$$f_m = \frac{G_m(9K_m + 8G_m)}{6(K_m + 2G_m)}, K_m = \frac{E_m}{3(1 - 2\nu_m)},$$

$$K_c = \frac{E_c}{3(1 - 2\nu_c)}, G_m = \frac{E_m}{2(1 + \nu_m)}, G_c = \frac{E_c}{2(1 + \nu_c)}, \quad (69)$$

where E_m and E_c are the Young moduli of metal and ceramic phases, ν_m and ν_c are the Poisson's ratios, G_m and G_c are the shear moduli, K_m and K_c are the bulk moduli, V_m and V_c are the volume fractions defined as:

$$V_m = 1 - V_c, \quad V_c = V_c^- + (V_c^+ - V_c^-)(0.5 + z)^\gamma, \quad z = x^3/h, \quad (70)$$

where V_c^- and V_c^+ are the volume fractions of the ceramic phase on the bottom and top surfaces and γ is the material gradient index.

It is supposed that the metal phase is aluminum with the material properties $E_m = 7 \times 10^{10}$ Pa and $\nu_m = 0.3$, whereas the material properties of the ceramic (SiC) are $E_c = 4.27 \times 10^{11}$ Pa and $\nu_c = 0.17$. The calculations were performed in the case of $V_c^- = 0$ and $\gamma = 2$ for three values of the volume fraction on the top surface $V_c^+ = 0, 0.4$ and 0.8 . The first value corresponds to the homogeneous plate. To analyze the results derived efficiently, we introduce dimensionless variables at point Q as functions of the thickness coordinate z as follows:

$$\bar{u}_i = E_m h u_i(Q, z)/F, \quad \bar{\sigma}_{\alpha\beta} = 10h^2 \sigma_{\alpha\beta}(Q, z)/F,$$

$$\bar{\sigma}_{i3} = 10^3 h^2 \sigma_{i3}(Q, z)/F, \quad (71)$$

where $h = 1$ m and $F = 1$ N.

Table 4 presents the data obtained by increasing the number of SaS inside the metal/ceramic plate with $V_c^+ = 0.8$

Table 4. Convergence study for a metal/ceramic trapezoidal plate with $V_c^+ = 0.8$ using 64×64 mesh.

Formulation	$\bar{u}_1(0.5)$	$\bar{u}_2(0.5)$	$\bar{u}_3(0.5)$	$\bar{\sigma}_{11}(0.5)$	$\bar{\sigma}_{11}(-0.5)$	$\bar{\sigma}_{22}(0.5)$	$\bar{\sigma}_{22}(-0.5)$	$\bar{\sigma}_{12}(0.5)$	$\bar{\sigma}_{12}(-0.5)$	$\bar{\sigma}_{13}(0)$	$\bar{\sigma}_{23}(0)$	$10\bar{\sigma}_{33}(0)$
$N = 3$	2.8841	1.2663	-2.1762	2.1131	0.73710	2.7363	0.86800	2.3326	0.80224	-1.4207	-3.4747	1.1735
$N = 5$	2.9171	1.2728	-2.0206	2.2904	0.72514	2.9840	0.83846	2.5629	0.76472	-1.9776	-4.4018	-9.2241
$N = 7$	2.9188	1.2732	-2.0158	2.3042	0.72448	3.0079	0.83545	2.5892	0.75893	-1.9867	-4.3327	-7.7464
$N = 9$	2.9189	1.2732	-2.0155	2.3052	0.72485	3.0102	0.83561	2.5924	0.75800	-1.9891	-4.3307	-7.9586
$N = 11$	2.9189	1.2732	-2.0155	2.3055	0.72465	3.0111	0.83532	2.5925	0.75819	-1.9889	-4.3310	-7.9308
$N = 13$	2.9189	1.2732	-2.0155	2.3052	0.72467	3.0105	0.83525	2.5929	0.75811	-1.9889	-4.3309	-7.9348

employing a mesh 64×64 . It is seen that the SaSQP4 element provides five right digits for displacements of the top surface using seven or nine SaS. Figure 5 displays the through-thickness distributions of displacements and stresses choosing nine SaS inside the plate body and the same fine mesh. These results show convincingly the high potential of the SaSQP4 element because the boundary conditions for transverse stresses on the bottom and top surfaces are satisfied correctly. The transverse stresses

are calculated through the constitutive equations without the use of any postprocessing procedures. Figure 6 presents the results of the convergence study due to mesh refinement for the homogeneous and metal/ceramic trapezoidal plates. As can be seen, the SaSQP4 element demonstrates good convergence characteristics even in the case of a metal/ceramic plate with $V_c^+ = 0.8$, except for the transverse shear stress $\bar{\sigma}_{13}$ that requires finer meshes.

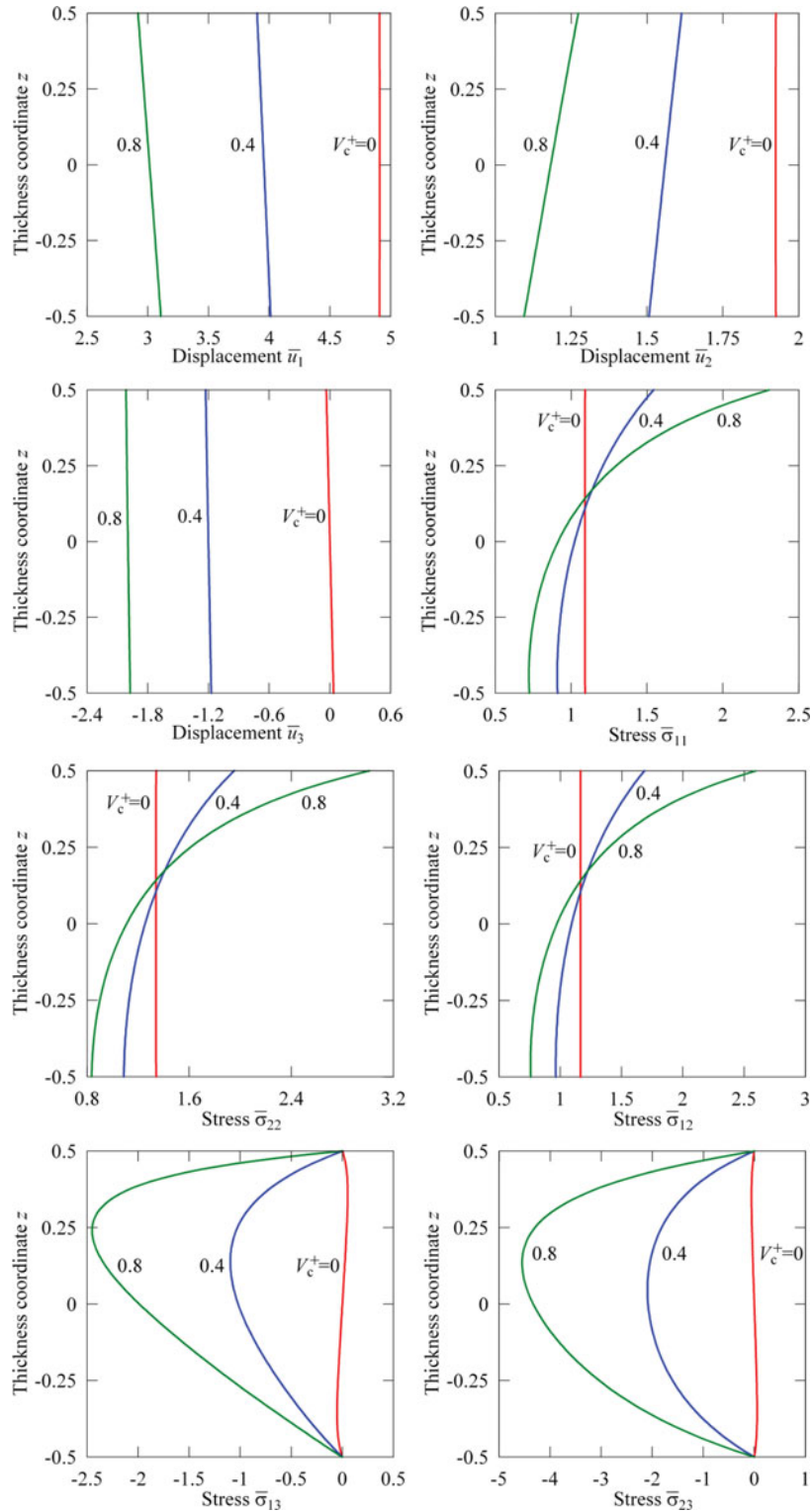


Figure 5. Through-thickness distributions of displacements and stresses for metal and metal/ceramic trapezoidal plates with $N = 9$ using 64×64 mesh.

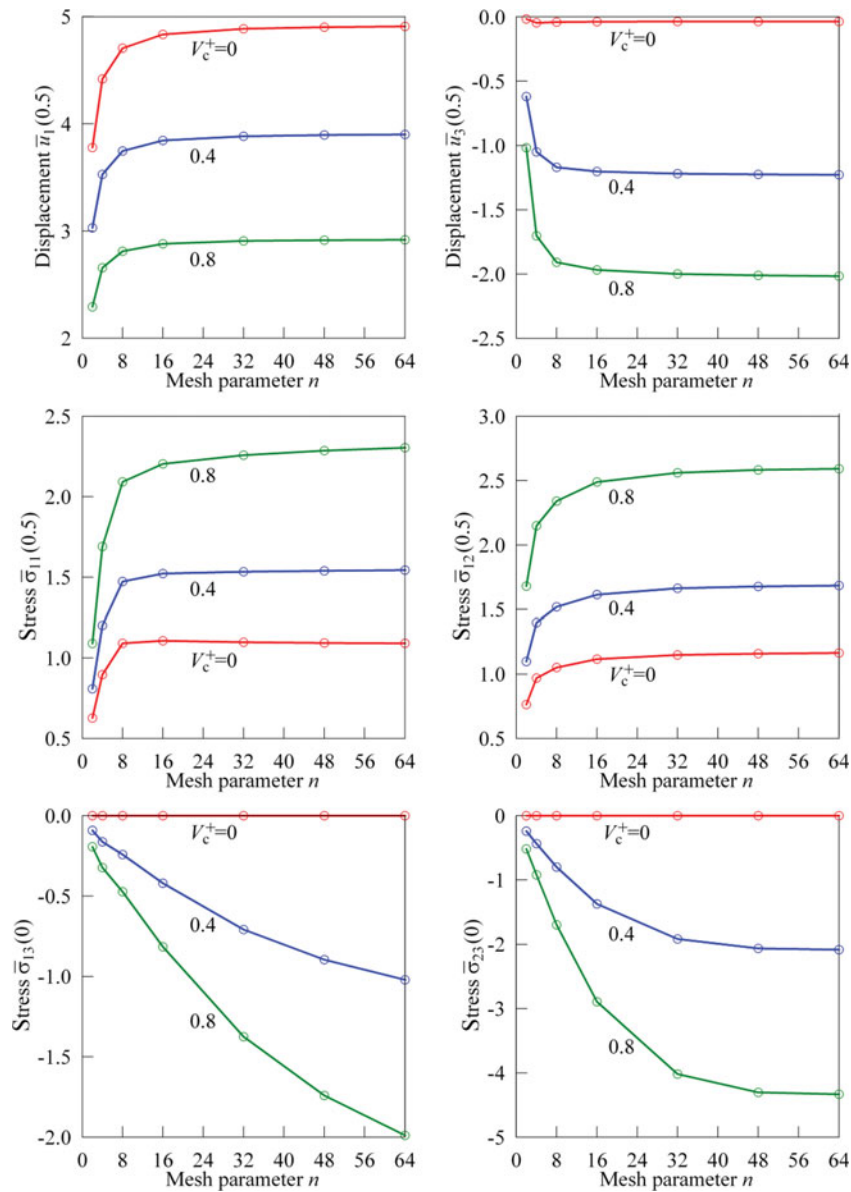


Figure 6. Results of the convergence study for metal and metal/ceramic trapezoidal plates with $N = 9$ by using $n \times n$ meshes of SaSQP4 elements.

6.3. Simply supported FG rectangular plate under sinusoidal loading

Consider a simply supported FG rectangular plate subjected to transverse sinusoidal loading acting on its top surface:

$$p_3^+ = p_0 \sin \frac{\pi x^1}{a} \sin \frac{\pi x^2}{b}, \quad p_3^- = 0, \quad (72)$$

where a and b are the plate dimensions.

Here, we study an FG plate composed of mixing the metal and ceramic phases. For evaluating the effective material properties through the thickness of the plate, the Mori–Tanaka method (69) with volume fractions (70) is adopted. The material properties of the metal and ceramic are given in the previous section. To compare the obtained results with the exact 3D solution of Vel and Batra [66], we accept $V_c^- = 0$, $V_c^+ = 0.5$ and $\gamma = 2$, and introduce dimensionless variables at crucial points as functions of the dimensionless thickness coordinate:

$$\begin{aligned} \bar{u}_1 &= 100h^2 E_m u_1(0, b/2, z)/a^3 p_0, \\ \bar{u}_3 &= 100h^3 E_m u_3(a/2, b/2, z)/a^4 p_0, \end{aligned}$$

$$\bar{\sigma}_{11} = 10h^2 \sigma_{11}(a/2, b/2, z)/a^2 p_0,$$

$$\bar{\sigma}_{12} = 10h^2 \sigma_{12}(0, 0, z)/a^2 p_0,$$

$$\bar{\sigma}_{13} = 10h \sigma_{13}(0, b/2, z)/a p_0,$$

$$\bar{\sigma}_{33} = \sigma_{33}(a/2, b/2, z)/p_0, \quad z = x^3/h, \quad (73)$$

where $a = b = 1$ m and $p_0 = 1$ Pa.

Due to symmetry, only one quarter of the plate is modeled by a uniform 64×64 mesh of SaSQP4 elements. The data listed in Tables 5 and 6 show that the SaSQP4 element allows reproducing the exact solution of elasticity [66] for thick and moderately thick plates with a very high accuracy utilizing the sufficiently large number of SaS inside the plate body and fine mesh configurations. As can be seen, the SaSQP4 element provides from four to six right digits for displacements and stresses of the thick metal/ceramic plate comparing to authors' exact SaS solution [33]. Figure 7 displays the distributions of displacements and stresses (73) through the thickness of the plate for different values of the slenderness ratio a/h by using nine SaS and the same 64×64 mesh. These results demonstrate again the high

Table 5. Convergence study for a metal/ceramic square plate with $a/h = 5$ using a uniform 64×64 mesh.

Formulation	$\bar{u}_1(0.5)$	$\bar{u}_1(-0.5)$	$\bar{u}_3(0.5)$	$\bar{u}_3(-0.5)$	$\bar{\sigma}_{11}(0.5)$	$\bar{\sigma}_{12}(0.5)$	$\bar{\sigma}_{13}(0)$	$\bar{\sigma}_{33}(0.5)$	$\bar{\sigma}_{33}(0.25)$
$N = 3$	2.83854	-3.69072	2.49155	2.38648	2.50140	-1.39688	-1.59062	0.92825	0.71246
$N = 5$	2.91258	-3.79891	2.55581	2.45422	2.74042	-1.55148	-2.29710	0.96932	0.81982
$N = 7$	2.91312	-3.79886	2.55597	2.45441	2.75575	-1.55951	-2.32038	0.99995	0.80993
$N = 9$	2.91313	-3.79885	2.55597	2.45441	2.75620	-1.55989	-2.31001	1.00000	0.80996
$N = 11$	2.91313	-3.79885	2.55597	2.45441	2.75623	-1.55991	-2.31002	1.00005	0.80995
Exact SaS [33]	2.91292		2.55588		2.75621	-1.55995	-2.31002		0.81001
Exact 3D [66]	2.9129		2.5559		2.7562	-1.5600	-2.3100		0.8100

Table 6. Convergence study for a metal/ceramic square plate with $a/h = 10$ using a uniform 64×64 mesh.

Formulation	$\bar{u}_1(0.5)$	$\bar{u}_1(-0.5)$	$\bar{u}_3(0.5)$	$\bar{u}_3(-0.5)$	$\bar{\sigma}_{11}(0.5)$	$\bar{\sigma}_{12}(0.5)$	$\bar{\sigma}_{13}(0)$	$\bar{\sigma}_{33}(0.5)$	$\bar{\sigma}_{33}(0.25)$
$N = 3$	2.87533	-3.73675	2.20245	2.18529	2.41288	-1.42037	-1.60132	0.04070	0.86013
$N = 5$	2.89946	-3.74759	2.21469	2.19824	2.63249	-1.54617	-2.30725	0.96893	0.82335
$N = 7$	2.89993	-3.74762	2.21485	2.19841	2.64199	-1.55252	-2.32395	0.99900	0.81188
$N = 9$	2.89994	-3.74762	2.21486	2.19841	2.64240	-1.55283	-2.32392	1.00054	0.81247
$N = 11$	2.89994	-3.74762	2.21486	2.19841	2.64242	-1.55285	-2.32392	1.00055	0.81247
Exact SaS [33]	2.89973		2.21480		2.64240	-1.55289	-2.32392		0.81231
Exact 3D [66]	2.8997		2.2148		2.6424	-1.5529	-2.3239		0.8123

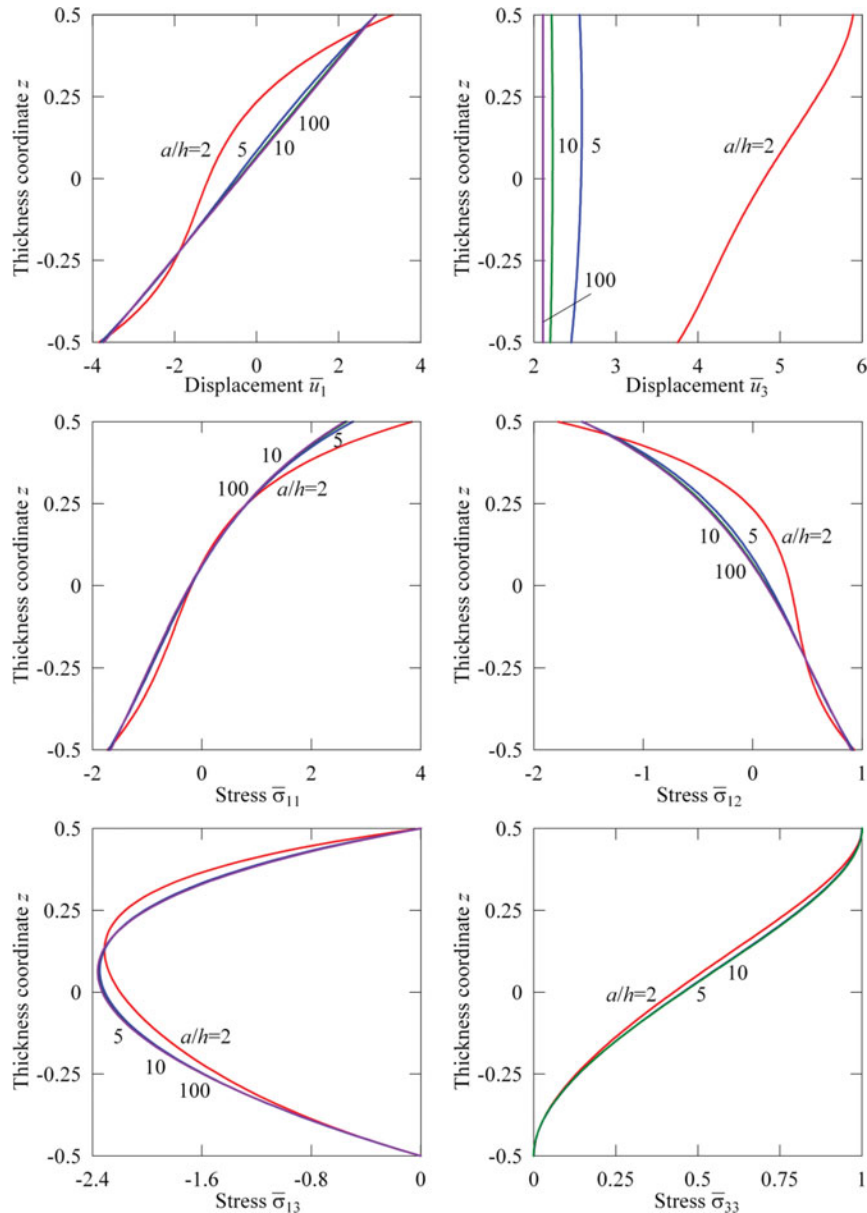


Figure 7. Through-the-thickness distributions of displacements and stresses of the simply supported metal/ceramic square plate with $N = 9$ using a uniform 64×64 mesh.

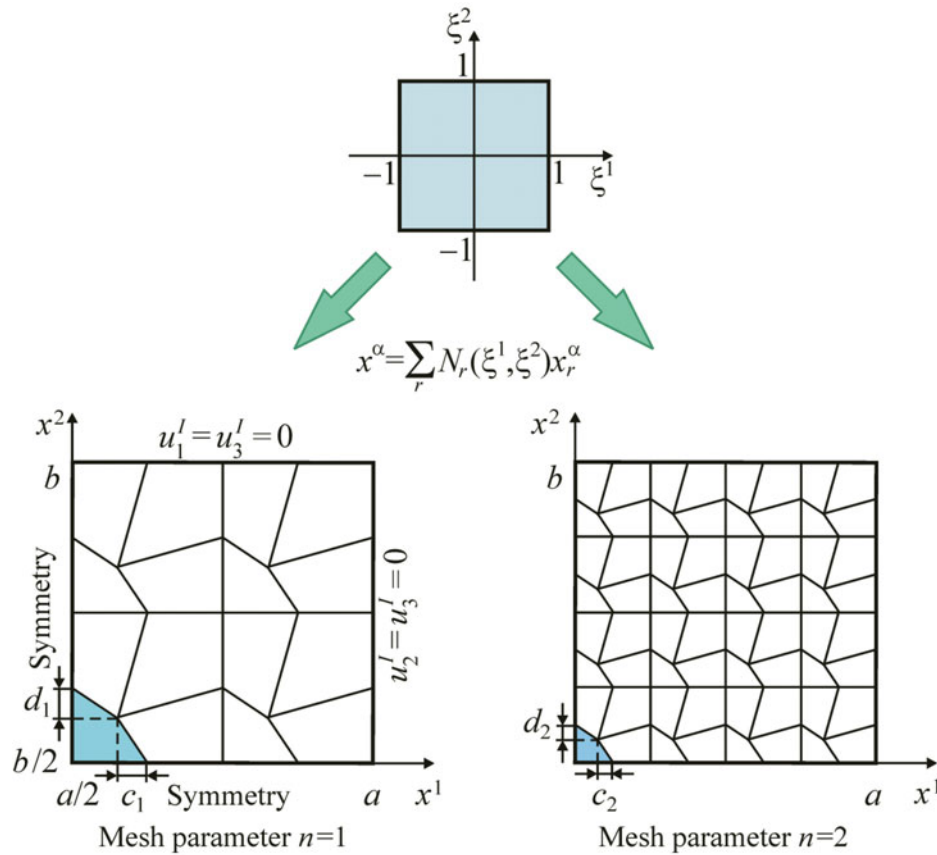


Figure 8. One quarter of the simply supported metal/ceramic square plate modeled by distorted $4n \times 4n$ meshes with $c_n = \delta a/8n$ and $d_n = \delta b/8n$, where $n = 1, 2, \dots, 16$ and $\delta \in [0, 0.6]$.

potential of the SaSQP4 element because the boundary conditions on the bottom and top surfaces for transverse stresses are satisfied properly.

To investigate the performance of the SaSQP4 element more carefully, we consider the distorted $4n \times 4n$ finite element meshes composed of $2n \times 2n$ squares with distorted 2×2 meshes inside them as depicted in Figure 8. The element mesh inside each square is distorted by moving the inner node along the diagonal. As a result, the generated meshes are defined by distortion parameters $c_n = \delta a/8n$ and $d_n = \delta b/8n$, which are dependent on a single distortion parameter $\delta \in [0, 0.6]$. Figures 9 and 10 show the results of the convergence study due to mesh refinement and mesh distortion through the use of normalized displacements and stresses for slenderness ratios of 10 and 100 by choosing nine SaS inside the plate. The analytical answers are provided by the exact SaS solution [33]. It is seen that the SaSQP4 element behaves practically insensitive with respect to the extremely high mesh distortion including $\delta = 0.6$ except for transverse stresses in the case of thin plates.

6.4. FG circular plate supported at two points

Here, we study a circular plate of the radius R supported at two diametrically opposite points and subjected to a concentrated load F at its center [67]. Such a problem is an excellent test to

verify the ability of the SaSQP4 element to model rigid-body motions and to assess additionally the effect of mesh distortion.

Owing to symmetry of the problem, one quarter of the plate is discretized by distorted meshes depicted in Figure 11. The geometrical and mechanical data of the plate are taken to be $R = 1$, $h = 0.01$, $E = 10^5$, $\nu = 0.25$ and $F = 1$. Table 7 shows the transverse displacement of the middle surface at points A and B for the different number of SaS by using a finite element mesh from Figure 11 with $n = 24$. A comparison with the analytical solution of the Kirchhoff plate theory [67] is presented because in the literature there is no available 3D analytical solution.

Finally, we consider an FG circular plate subjected to a concentrated load F at its center on the top surface. The plate is made of the transversely isotropic material with material properties distributed in the thickness direction according to a power law:

$$C_{ijkl} = C_{ijkl}^- V^- + C_{ijkl}^+ V^+, \quad C_{ijkl}^+ = 2C_{ijkl}^-,$$

$$V^+ = 1 - V^-, \quad V^- = (0.5 - z)^\gamma, \quad -0.5 \leq z \leq 0.5, \quad (74)$$

where C_{ijkl}^- and C_{ijkl}^+ are the elastic constants on the bottom and top surfaces, γ is the material gradient index, $z = x^3/h$ is the dimensionless thickness coordinate. The elastic constants on the

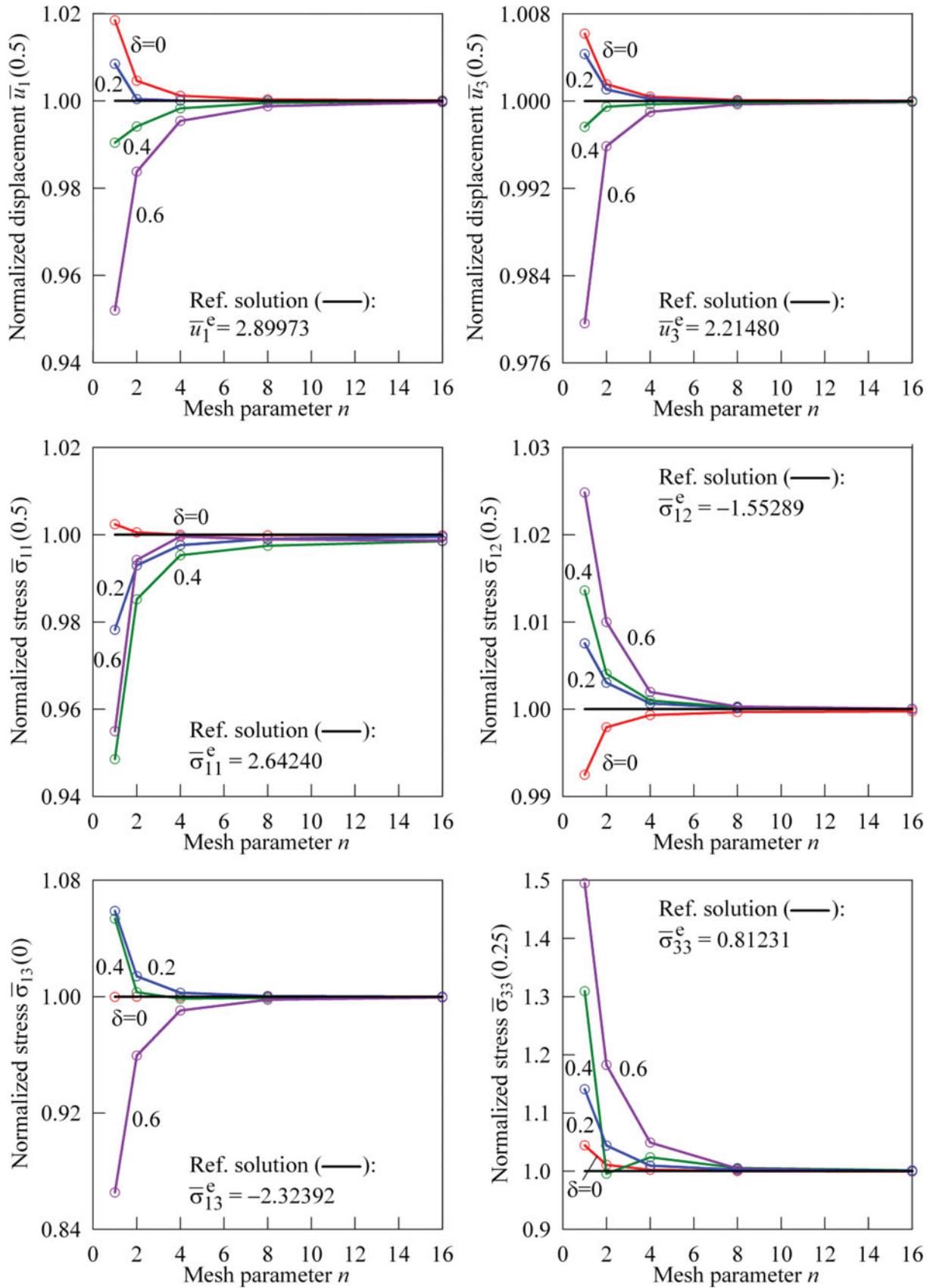


Figure 9. Convergence study due to mesh refinement and mesh distortion for a simply supported metal/ceramic square plate with $a/h = 10$ and $N = 9$.

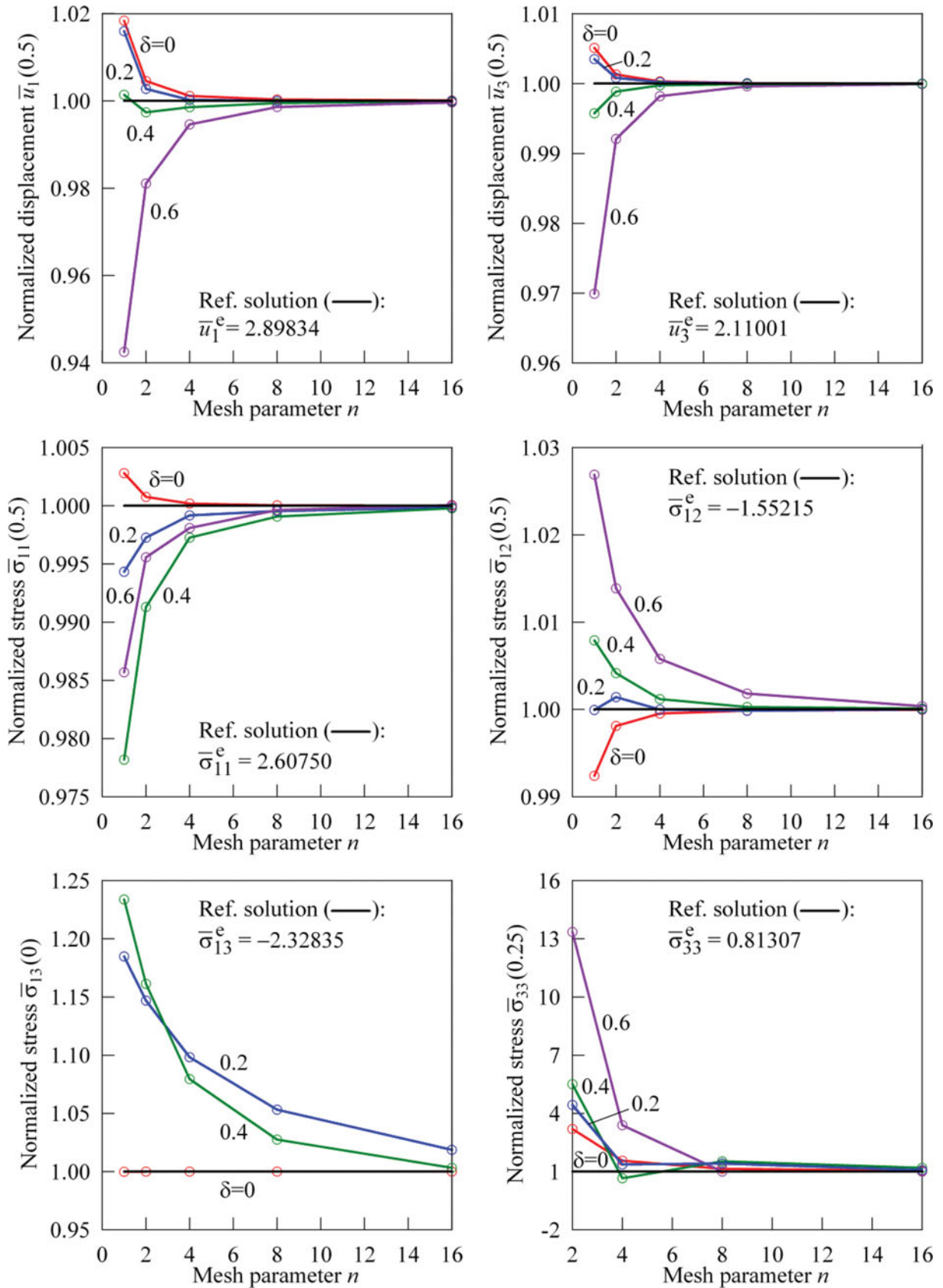


Figure 10. Convergence study due to mesh refinement and mesh distortion for a simply supported metal/ceramic square plate with $a/h = 100$ and $N = 9$.

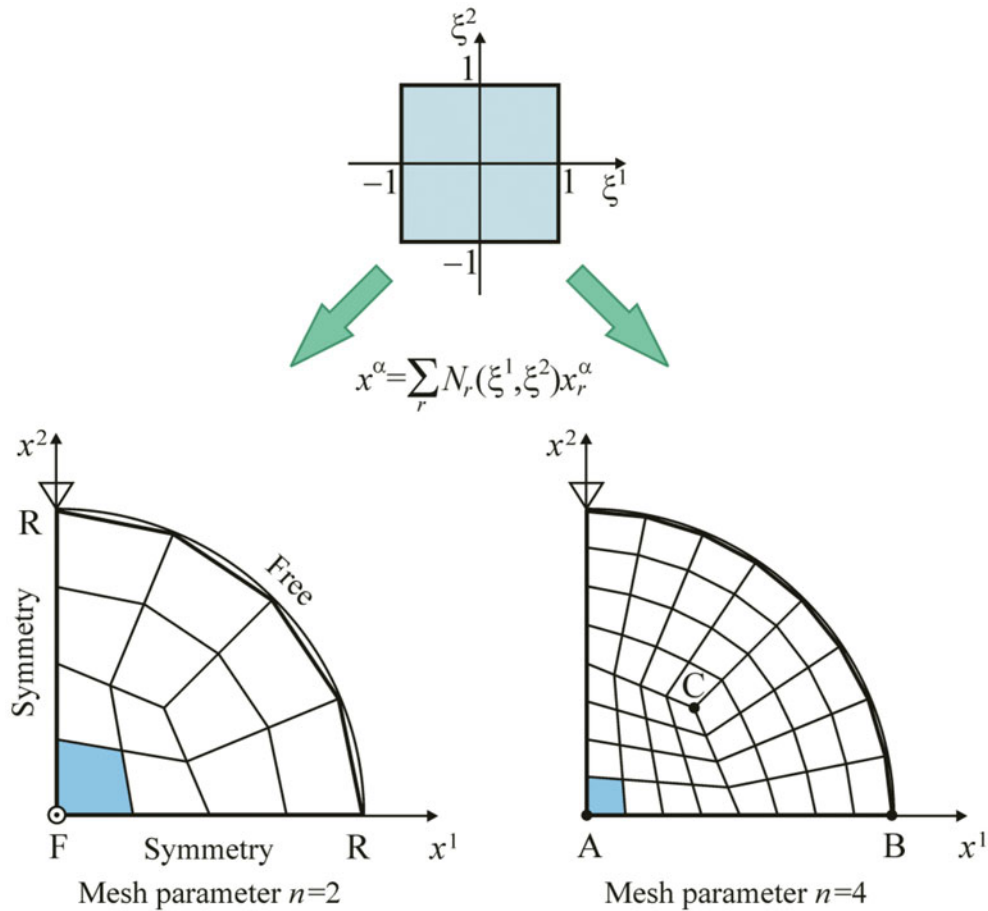


Figure 11. One quarter of the circular plate supported at two points under a concentrated load at the center modeled by distorted meshes with $3n^2$ elements, where $n = 2, 4, \dots, 24$.

Table 7. Transverse displacement $\bar{u}_3(P) = Eh^3u_3(P, 0)/R^2F$ at any point $P(x^1, x^2)$ belonging to the middle surface of the homogeneous circular plate supported at two points with $R/h = 100$ using a mesh from Figure 11 with $n = 24$.

Formulation	$N = 3$	$N = 5$	$N = 7$	Kirchhoff plate [67]
$\bar{u}_3(A)$	1.3134	1.3135	1.3135	1.31
$\bar{u}_3(B)$	1.3290	1.3292	1.3292	1.33

bottom surface are:

$$\begin{aligned}
 C_{1111}^- &= C_{2222}^- = 41.3 \text{ GPa}, & C_{1122}^- &= 14.7 \text{ GPa}, \\
 C_{1133}^- &= C_{2233}^- = 10.1 \text{ GPa}, & C_{3333}^- &= 36.2 \text{ GPa}, \\
 C_{1313}^- &= C_{2323}^- = 10.0 \text{ GPa}, & C_{1212}^- &= 13.3 \text{ GPa}.
 \end{aligned}$$

Due to symmetry, only one quarter of the plate with $R = 1$ m and $\gamma = 2$ is modeled by distorted meshes from Figure 11. It is convenient to introduce dimensionless variables at any point

$P(x^1, x^2)$ belonging to the middle surface as functions of the dimensionless thickness coordinate as follows:

$$\begin{aligned}
 \bar{u}_1(P) &= 10^3 C_{1313}^- hu_1(P, z)/SF, \\
 \bar{u}_2(P) &= 100 C_{1313}^- hu_2(P, z)/SF, \\
 \bar{u}_3(P) &= 10 C_{1313}^- hu_3(P, z)/S^2F, \\
 \bar{\sigma}_{11}(P) &= 100h^2\sigma_{11}(P, z)/F, & \bar{\sigma}_{22}(P) &= h^2\sigma_{22}(P, z)/F, \\
 \bar{\sigma}_{12}(P) &= 10h^2\sigma_{12}(P, z)/F, & \bar{\sigma}_{\alpha 3}(P) &= 10Sh^2\sigma_{\alpha 3}(P, z)/F,
 \end{aligned} \tag{75}$$

where $F = 1$ N and $S = R/h$ is the slenderness ratio.

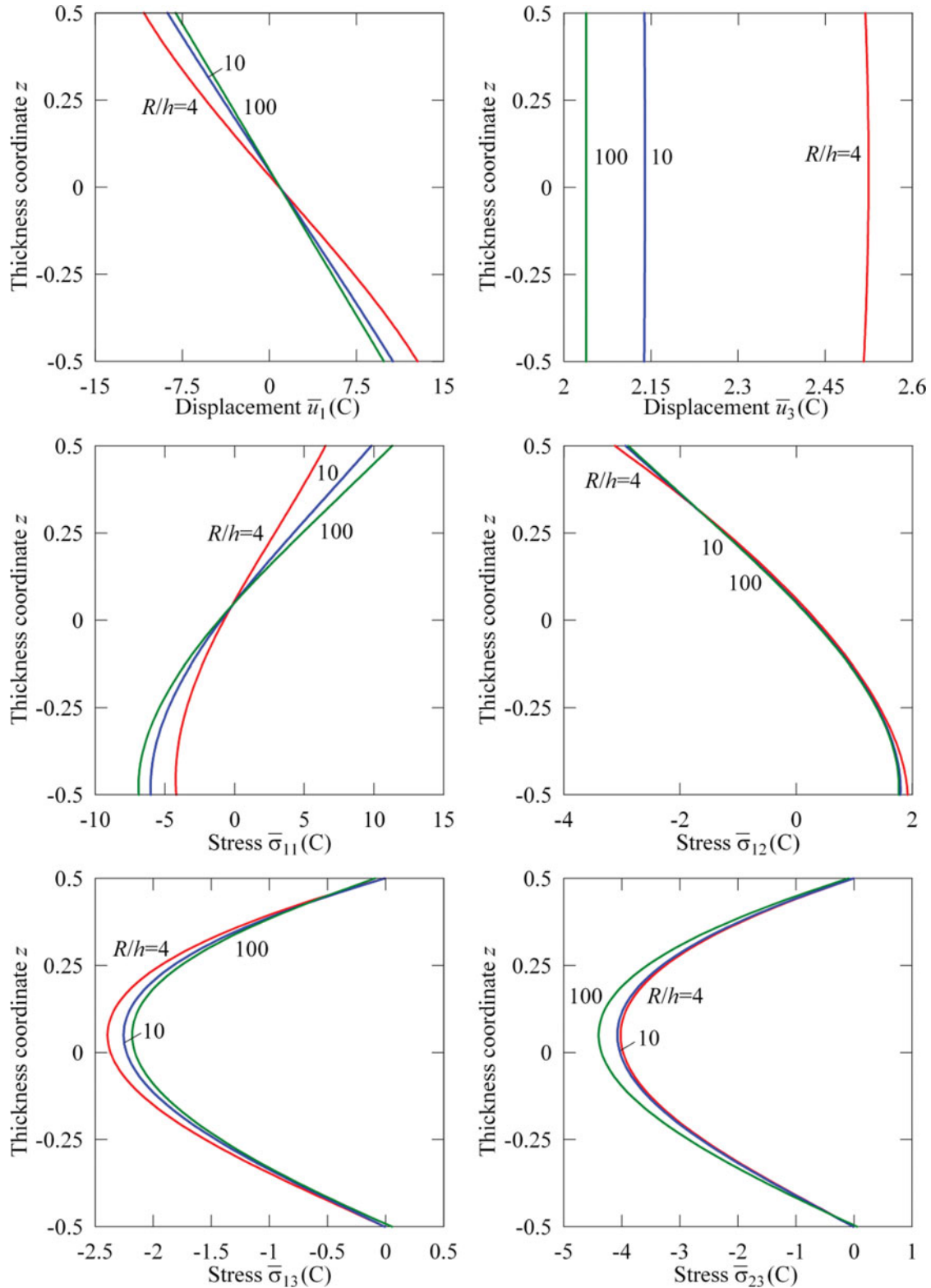
Tables 8 and 9 list the displacements and stresses at points $A(0, 0)$, $B(1, 0)$ and $C(\sqrt{2}/4, \sqrt{2}/4)$ for the different number of SaS by using a mesh from Figure 11 with $n = 20$. Figure 12 displays the through-thickness distributions of displacements and stresses at point C for three values of the

Table 8. Convergence study for an FG circular plate supported at two points with $R/h = 4$ using a mesh from Figure 11 with $n = 20$.

Formulation	$\bar{u}_1(C, 0.5)$	$\bar{u}_2(C, 0.5)$	$\bar{u}_3(A, 0)$	$\bar{u}_3(B, 0)$	$\bar{u}_3(C, 0)$	$\bar{\sigma}_{11}(C, 0.5)$	$\bar{\sigma}_{22}(C, 0.5)$	$\bar{\sigma}_{12}(C, 0.5)$	$\bar{\sigma}_{13}(C, 0)$	$\bar{\sigma}_{23}(C, 0)$
$N = 3$	-10.888	7.9396	2.8665	3.0403	2.4667	7.2130	1.3731	-3.1127	-1.7042	-2.8766
$N = 5$	-10.796	8.0251	3.1092	3.0889	2.5108	6.4697	1.3324	-3.1290	-2.3705	-3.9886
$N = 7$	-10.799	8.0253	3.0405	3.0912	2.5131	6.4722	1.3324	-3.1265	-2.3524	-3.9601
$N = 9$	-10.799	8.0253	3.0615	3.0917	2.5135	6.4749	1.3325	-3.1263	-2.3538	-3.9624

Table 9. Convergence study for an FG circular plate supported at two points with $R/h = 10$ using a mesh from Figure 11 with $n = 20$.

Formulation	$\bar{u}_1(C, 0.5)$	$\bar{u}_2(C, 0.5)$	$\bar{u}_3(A, 0)$	$\bar{u}_3(B, 0)$	$\bar{u}_3(C, 0)$	$\bar{\sigma}_{11}(C, 0.5)$	$\bar{\sigma}_{22}(C, 0.5)$	$\bar{\sigma}_{12}(C, 0.5)$	$\bar{\sigma}_{13}(C, 0)$	$\bar{\sigma}_{23}(C, 0)$
$N = 3$	-8.7516	7.8420	2.5350	2.6686	2.1269	10.240	1.3546	-3.0228	-1.5986	-2.9213
$N = 5$	-8.7614	7.8578	2.5572	2.6802	2.1369	9.7617	1.3105	-2.9417	-2.2290	-4.0470
$N = 7$	-8.7619	7.8579	2.5568	2.6804	2.1372	9.7649	1.3105	-2.9411	-2.2126	-4.0170
$N = 9$	-8.7618	7.8579	2.5567	2.6805	2.1372	9.7678	1.3108	-2.9407	-2.2128	-4.0183

**Figure 12.** Through-the-thickness distributions of displacements and stresses for an FG circular plate supported at two points for $N = 7$ using a distorted mesh from Figure 11 with $n = 24$.

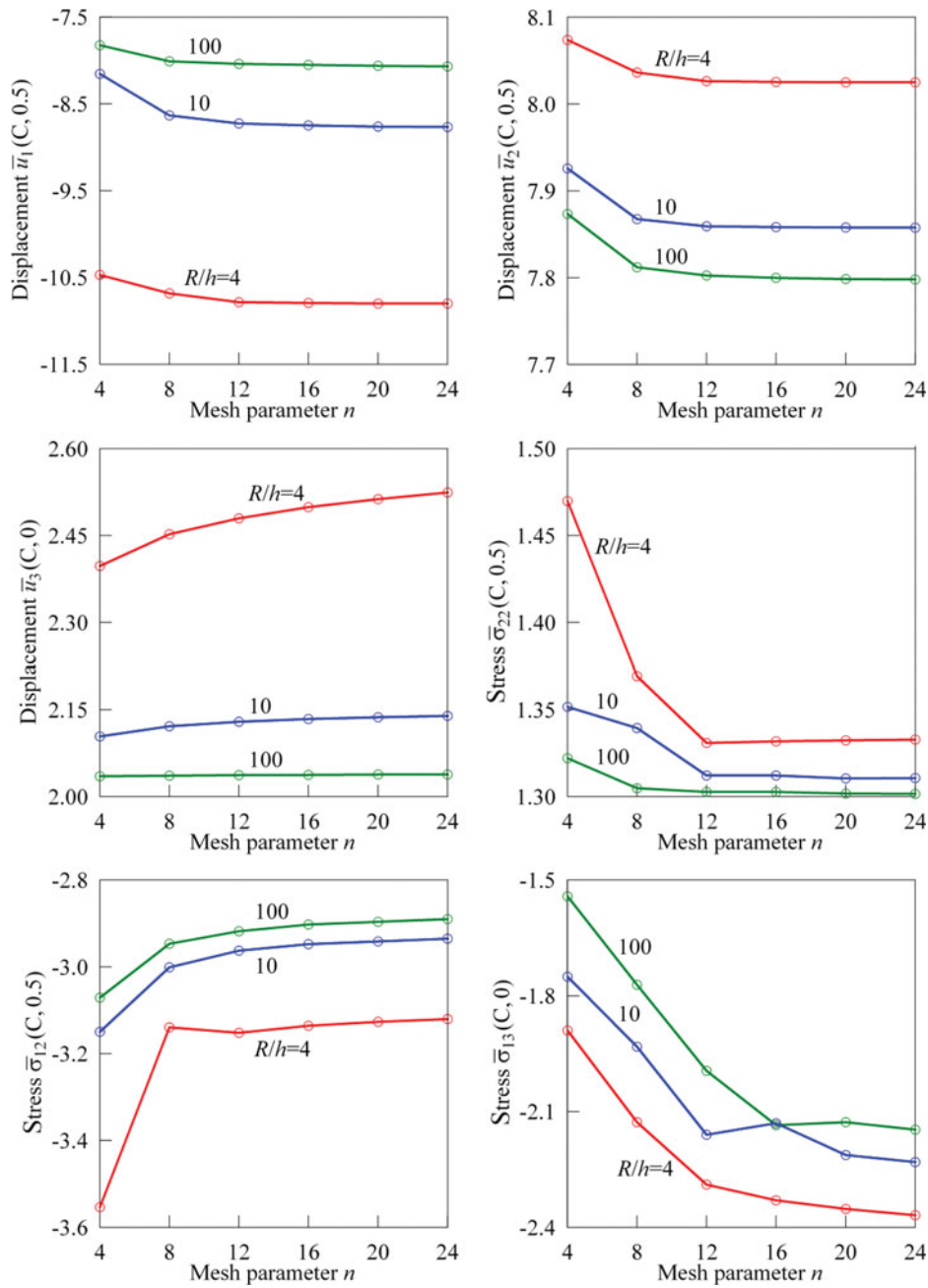


Figure 13. Convergence study due to mesh refinement for an FG circular plate supported at two points for $N = 7$ using distorted meshes from Figure 11.

slenderness ratio S employing seven SaS and a mesh with $n = 24$. It is seen that the boundary conditions for transverse stresses on the bottom and top surfaces are satisfied again correctly, especially for thick plates. Figure 13 shows the results of the convergence study due to mesh refinement through displacements and stresses of the middle surface or the top surface at point C taking seven SaS inside the plate body. One can see that the SaSQP4 element represents rigid-body plate motions properly, and it is free from locking in thin plate limits.

7. Conclusions

The article describes a hybrid-mixed ANS four-node quadrilateral element based on the SaS formulation in which the

displacement vectors of SaS are utilized as basic plate unknowns. The SaS are located at Chebyshev polynomial nodes inside the plate body that make it possible to minimize uniformly the error because of the Lagrange interpolation of displacements, strains and material properties through the thickness. It is important that the element stiffness matrix is evaluated without using the expensive numerical matrix inversion that is impossible in available hybrid-mixed finite element formulations. The SaSQP4 element developed passes 3D patch tests for the FG plates and exhibits a superior performance in the case of coarse distorted mesh configurations for all 3D benchmarks considered. It can be recommended for the 3D stress analysis of thin and thick FG plates due to the fact that the SaS solutions asymptotically approach the solutions of elasticity as the number of SaS goes to infinity.

Funding

This work was supported by the Russian Science Foundation (grant no. 15-19-30002) and the Russian Ministry of Education and Science (grant no. 9.4914.2017).

References

- [1] Y. Tanigawa, Some basic thermoelastic problems for nonhomogeneous structural materials, *Appl. Mech. Rev.*, vol. 48, pp. 287–300, 1995.
- [2] N. Noda, Thermal stresses in functionally graded materials, *J. Therm. Stress.*, vol. 22, pp. 477–512, 1999.
- [3] V. Birman and L.W. Byrd, Modeling and analysis of functionally graded materials and structures, *Appl. Mech. Rev.*, vol. 60, pp. 195–216, 2007.
- [4] D.K. Jha, T. Kant, and R.K. Singh, A critical review of recent research on functionally graded plates, *Compos. Struct.*, vol. 96, pp. 833–849, 2013.
- [5] K. Swaminathan, D.T. Naveenkumar, A.M. Zenkour, and E. Carrera, Stress, vibration and buckling analyses of FGM plates—A state-of-the-art review, *Compos. Struct.*, vol. 120, pp. 10–31, 2015.
- [6] G. Praveen and J.N. Reddy, Nonlinear transient thermoelastic analysis of functionally graded ceramic-metal plates, *Int. J. Solids Struct.*, vol. 35, pp. 4457–4476, 1998.
- [7] L.D. Croce and P. Venini, Finite elements for functionally graded Reissner-Mindlin plates, *Comput. Methods Appl. Mech. Eng.*, vol. 193, pp. 705–725, 2004.
- [8] C. Chinosi and L.D. Croce, Approximation of functionally graded plates with non-conforming finite elements, *J. Comput. Appl. Math.*, vol. 210, pp. 106–115, 2007.
- [9] H. Nguyen-Xuan, L.V. Tran, C.H. Thai, and T. Nguyen-Thoi, Analysis of functionally graded plates by an efficient finite element method with node-based strain smoothing, *Thin-Walled Struct.*, vol. 54, pp. 1–18, 2012.
- [10] G. Castellazzi, C. Gentilini, P. Krysl, and I. Elishakoff, Static analysis of functionally graded plates using a nodal integrated finite element approach, *Compos. Struct.*, vol. 103, pp. 197–200, 2013.
- [11] N. Valizadeh, S. Natarajan, O.A. Gonzalez-Estrada, T. Rabczuk, T.Q. Bui, and S.P.A. Bordas, NURBS-based finite element analysis of functionally graded plates: Static bending, vibration, buckling and flutter, *Compos. Struct.*, vol. 99, pp. 309–326, 2013.
- [12] N. El-Abbasi and S.A. Meguid, Finite element modeling of the thermoelastic behavior of functionally graded plates and shells, *Int. J. Comp. Eng. Sci.*, vol. 1, pp. 151–165, 2000.
- [13] N. El-Abbasi and S.A. Meguid, A new shell element accounting for through-thickness deformation, *Comput. Methods Appl. Mech. Eng.*, vol. 189, pp. 841–862, 2000.
- [14] R.A. Arciniega and J.N. Reddy, Large deformation analysis of functionally graded shells, *Int. J. Solids Struct.*, vol. 44, pp. 2036–2052, 2007.
- [15] J.N. Reddy, Analysis of functionally graded plates, *Int. J. Numer. Meth. Eng.*, vol. 47, pp. 663–684, 2000.
- [16] W. Zhen and C. Wanji, A higher-order theory and refined three-node triangular element for functionally graded plates, *Eur. J. Mech. A/Solids*, vol. 25, pp. 447–463, 2006.
- [17] S. Pradyumna, N. Nanda, and J.N. Bandyopadhyay, Geometrically nonlinear transient analysis of functionally graded shell panels using a higher-order finite element formulation, *J. Mech. Eng. Res.*, vol. 2, pp. 39–51, 2010.
- [18] S. Natarajan and G. Manickam, Bending and vibration of functionally graded material sandwich plates using an accurate theory, *Finite Elem. Anal. Des.*, vol. 57, pp. 32–42, 2012.
- [19] M.N.A. Gulshan Taj, A. Chakrabarti, and A.H. Sheikh, Analysis of functionally graded plates using higher order shear deformation theory, *Appl. Math. Model.*, vol. 37, pp. 8484–8494, 2013.
- [20] H.T. Thai and D.H. Choi, Finite element formulation of various four unknown shear deformation theories for functionally graded plates, *Finite Elem. Anal. Des.*, vol. 75, pp. 50–61, 2013.
- [21] L.V. Tran, A.J.M. Ferreira, and H. Nguyen-Xuan, Isogeometric analysis of functionally graded plates using higher-order shear deformation theory, *Compos. Part B Eng.*, vol. 51, pp. 368–383, 2013.
- [22] M. Talha and B.N. Singh, Static response and free vibration analysis of FGM plates using higher order shear deformation theory, *Appl. Math. Model.*, vol. 34, pp. 3991–4011, 2010.
- [23] C.H. Thai, A.M. Zenkour, M.A. Wahab, and H. Nguyen-Xuan, A simple four-unknown shear and normal deformations theory for functionally graded isotropic and sandwich plates based on isogeometric analysis, *Compos. Struct.*, vol. 139, pp. 77–95, 2016.
- [24] M. Cinefra, E. Carrera, L.D. Croce, and C. Chinosi, Refined shell elements for the analysis of functionally graded structures, *Compos. Struct.*, vol. 94, pp. 415–422, 2012.
- [25] E. Carrera, Theories and finite elements for multilayered, anisotropic, composite plates and shells, *Arch. Comput. Meth. Eng.*, vol. 9, pp. 1–60, 2002.
- [26] E. Carrera, Theories and finite elements for multilayered plates and shells: A unified compact formulation with numerical assessment and benchmarking, *Arch. Comput. Meth. Eng.*, vol. 10, pp. 215–296, 2003.
- [27] G.M. Kulikov and E. Carrera, Finite deformation higher-order shell models and rigid-body motions, *Int. J. Solids Struct.*, vol. 45, pp. 3153–3172, 2008.
- [28] G.M. Kulikov and S.V. Plotnikova, Exact 3D stress analysis of laminated composite plates by sampling surfaces method, *Compos. Struct.*, vol. 94, pp. 3654–3663, 2012.
- [29] G.M. Kulikov and S.V. Plotnikova, A new approach to three-dimensional exact solutions for functionally graded piezoelectric laminated plates, *Compos. Struct.*, vol. 106, pp. 33–46, 2013.
- [30] M. Darabi and R. Ganesan, Exact 3-D stress and stiffness analysis of functionally graded sandwich plates using sampling surfaces method, *Proceedings of the ASME International Mechanical Engineering Congress and Exposition: Mechanics of Solids, Structures and Fluids*, vol. 9. V009T12A065, pp. 1–11, November 14–20, Montreal, QC, 2014.
- [31] M. Darabi and V. Ganesan, Exact 3-D stress and stiffness analysis of functionally graded cylindrical shells, *Proceedings of the Tenth joint Canada-Japan Workshop on Composites: Design, Manufacturing and Applications of Composites*, pp. 172–184, August 19–21, Vancouver, Canada, 2015.
- [32] G.M. Kulikov and S.V. Plotnikova, A sampling surfaces method and its implementation for 3D thermal stress analysis of functionally graded plates, *Compos. Struct.*, vol. 120, pp. 315–325, 2015.
- [33] G.M. Kulikov and S.V. Plotnikova, Three-dimensional analysis of metal-ceramic shells by the method of sampling surfaces, *Mech. Compos. Mater.*, vol. 51, pp. 455–464, 2015.
- [34] G.M. Kulikov and S.V. Plotnikova, Sampling surfaces formulation for thermoelastic analysis of laminated functionally graded shells, *Mechanica*, vol. 51, pp. 1913–1929, 2016.
- [35] C. Runge, Über empirische Funktionen und die Interpolation zwischen äquidistanten Ordinaten, *Z. Math. Physik.*, vol. 46, pp. 224–243, 1901.
- [36] R.L. Burden and J.D. Faires, *Numerical Analysis*. 9th ed., Brooks/Cole, Cengage Learning, Boston, 2010.
- [37] T.J.R. Hughes and T.E. Tezduyar, Finite elements based upon Mindlin plate theory with particular reference to the four-node bilinear isoparametric element, *J. Appl. Mech.*, vol. 48, pp. 587–596, 1981.
- [38] R.H. MacNeal, Derivation of element stiffness matrices by assumed strain distributions, *Nucl. Eng. Des.*, vol. 70, pp. 3–12, 1982.
- [39] K.J. Bathe and E.N. Dvorkin, A four-node plate bending element based on Mindlin/Reissner plate theory and a mixed interpolation, *Int. J. Numer. Meth. Eng.*, vol. 21, pp. 367–383, 1985.
- [40] T.J.R. Hughes, *The Finite Element Method: Linear Static and Dynamic Finite Element Analysis*, Prentice-Hall, Englewood Cliffs, NJ, 1987.
- [41] K.J. Bathe, *Finite Element Procedures*, Prentice-Hall, Upper Saddle River, NJ, 1996.
- [42] T.H.H. Pian, Derivation of element stiffness matrices by assumed stress distributions, *AIAA J.*, vol. 2, pp. 1333–1336, 1964.
- [43] T.H.H. Pian and K. Sumihara, Rational approach for assumed stress finite elements, *Int. J. Numer. Meth. Eng.*, vol. 20, pp. 1685–1695, 1984.

- [44] K.Y. Sze, W.K. Chan, and T.H.H. Pian, An eight-node hybrid-stress solid-shell element for geometric non-linear analysis of elastic shells, *Int. J. Numer. Meth. Eng.*, vol. 55, pp. 853–878, 2002.
- [45] S.W. Lee and T.H.H. Pian, Improvement of plate and shell finite elements by mixed formulations, *AIAA J.*, vol. 16, pp. 29–34, 1978.
- [46] H.C. Park, C. Cho, and S.W. Lee, An efficient assumed strain element model with six DOF per node for geometrically non-linear shells, *Int. J. Numer. Meth. Eng.*, vol. 38, pp. 4101–4122, 1995.
- [47] G. Wempner, D. Talaslidis, and C.M. Hwang, A simple and efficient approximation of shells via finite quadrilateral elements, *J. Appl. Mech.*, vol. 49, pp. 115–120, 1982.
- [48] G.M. Kulikov and S.V. Plotnikova, Non-linear exact geometry 12-node solid-shell element with three translational degrees of freedom per node, *Int. J. Numer. Meth. Eng.*, vol. 88, pp. 1363–1389, 2011.
- [49] T.H.H. Pian, State-of-the-art development of hybrid/mixed finite element method, *Finite Elem. Anal. Des.*, vol. 21, pp. 5–20, 1995.
- [50] S.V. Hoa and W. Feng, *Hybrid Finite Element Method for Stress Analysis of Laminated Composites*, Springer Science, New York, 1998.
- [51] G.M. Kulikov and S.V. Plotnikova, On the use of a new concept of sampling surfaces in a shell theory, *Adv. Structured Mater.*, vol. 15, pp. 715–726, 2011.
- [52] G.M. Kulikov and S.V. Plotnikova, A method of solving three-dimensional problems of elasticity for laminated composite plates, *Mech. Compos. Mater.*, vol. 48, pp. 15–26, 2012.
- [53] G.M. Kulikov and S.V. Plotnikova, A hybrid-mixed four-node quadrilateral plate element based on sampling surfaces method for 3D stress analysis, *Int. J. Numer. Meth. Eng.*, vol. 108, pp. 26–54, 2016.
- [54] G.M. Kulikov and S.V. Plotnikova, Solution of three-dimensional problems for thick elastic shells by the method of reference surfaces, *Mech. Solids*, vol. 49, pp. 403–412, 2014.
- [55] K. Washizu, *Variational Methods in Elasticity and Plasticity*. 3rd ed., Pergamon, Oxford, 1982.
- [56] J.C. Simo, D.D. Fox, and M.S. Rifai, On a stress resultant geometrically exact shell model. Part II: The linear theory; computational aspects, *Comput. Methods Appl. Mech. Eng.*, vol. 73, pp. 53–92, 1989.
- [57] J.C. Simo, M.S. Rifai, and D.D. Fox, On a stress resultant geometrically exact shell model. Part IV: Variable thickness shells with through-the-thickness stretching, *Comput. Methods Appl. Mech. Eng.*, vol. 81, pp. 91–126, 1990.
- [58] G.M. Kulikov and S.V. Plotnikova, A family of ANS four-node exact geometry shell elements in general convected curvilinear coordinates, *Int. J. Numer. Meth. Eng.*, vol. 83, pp. 1376–1406, 2010.
- [59] G.M. Kulikov and S.V. Plotnikova, Hybrid-mixed ANS finite elements for stress analysis of laminated composite structures: Sampling surfaces plate formulation, *Comput. Methods Appl. Mech. Eng.*, vol. 303, pp. 374–399, 2016.
- [60] R.H. MacNeal and R.L. Harder, A proposed standard set of problems to test finite element accuracy, *Finite Elem. Anal. Des.*, vol. 1, pp. 3–20, 1985.
- [61] R.D. Cook, Improved two-dimensional finite element, *J. Struct. Div. ASCE*, vol. 100, pp. 1851–1863, 1974.
- [62] A. Cazzani and S.N. Atluri, Four-noded mixed finite elements, using unsymmetric stresses, for linear analysis of membranes, *Comput. Mech.*, vol. 11, pp. 229–251, 1993.
- [63] U. Hueck and P. Wriggers, A formulation for the 4-node quadrilateral element, *Int. J. Numer. Meth. Eng.*, vol. 38, pp. 3007–3037, 1995.
- [64] T. Mori and K. Tanaka, Average stress in matrix and average elastic energy of materials with misfitting inclusions, *Acta Metall.*, vol. 21, pp. 571–574, 1973.
- [65] Y. Benveniste, A new approach to the application of Mori–Tanaka’s theory in composite materials, *Mech. Mater.*, vol. 6, pp. 147–157, 1987.
- [66] S.S. Vel and R.C. Batra, Exact solution for thermoelastic deformations of functionally graded thick rectangular plates, *AIAA J.*, vol. 40, pp. 1421–1433, 2002.
- [67] S.P. Timoshenko and S. Woinowsky-Krieger, *Theory of Plates and Shells*. 2nd ed., McGraw-Hill, New York, 1970.